SIMULATION OF MECHANICAL, THERMODYNAMIC, AND MAGNETIC PROPERTIES OF MAGNESIA WITH SUBSTITUTIONAL ELEMENTS FOR IMPROVED MAGNETIC CORE COATING APPLICATIONS

A Thesis

Submitted to the Faculty

of

Purdue University

by

Asimiyu A. Tiamiyu

In Partial Fulfillment of the

Requirements for the Degree

of

Master of Science in Mechanical Engineering

December 2019

Purdue University

Indianapolis, Indiana

THE PURDUE UNIVERSITY GRADUATE SCHOOL
STATEMENT OF THESIS APPROVAL

Dr. Jing Zhang, Chair

Department of Mechanical and Energy Engineering

Dr. Xiaoliang Wei

Department of Mechanical and Energy Engineering

Dr. Shengfeng Yang

Department of Mechanical and Energy Engineering

Approved by:

Dr. Sohel Anwar

Head of the School Graduate Program

In Dedication to God and my lovely family - Morufat, Amir, Amirah Tiamiyu.

ACKNOWLEDGMENTS

The author would like to appreciate Dr. Jing Zhang for mentoring my research work. I also would like to extend thanks to Dr. Xiaoliang Wei and Dr. Shengfeng Yang for serving on my thesis committee. The author also thanks Professor Yeon-Gil Jung from Changwon National University for acquiring the SEM/EDS and XRD data, and Bonggu Kim for helping with the analyses of the SEM/EDS and XRD results.

TABLE OF CONTENTS

Page

Page

LIST OF TABLES

LIST OF FIGURES

Figure Page

SYMBOLS

ϕ	magnetic flux
ϕ_{max}	maximum magnetic flux
B	magnetic flux density
M_c	magnetization of core
μ_o	permeability of free space
μ_{ion}	net magnetic moment
e	induced voltage
P_{eddy}	eddy current loss
R_{path}	path resistance
ρ	resistivity
ω	angular frequency
θ	angular displacement
ε	shear strain
M	moment
C_{ij}	elastic constant
t	time
I_{max}	peak current
E_{max}	maximum induced voltage
A	area
τ	plate thickness
R	resistance
σ_{cd}	conductivity
P_h	hysteresis loss
H_v	Vicker hardness

σ	stress
G	shear modulus
m	mass
f_i	interatomic force
$\ddot{r}_i$	interatomic acceleration
U_i	interatomic energy
σ_c	compressive strength
m	mass
F_{load}	loading force
F_{unload}	unloading force
U	internal energy
T	temperature
S	entropy
G	Gibbs free enegy
P	pressure
V	volume
F_z	Helmholtz free energy
d	lattice spacing
μ	magnetic moment
S_n	spin quantum summation
$\dot{Q}$	heat transferred rate

ABSTRACT

Tiamiyu, Asimiyu A. M.S., Purdue University, December 2019. Simulation of Mechanical, Thermodynamic, and Magnetic Properties of Magnesia with Substitutional Elements for Improved Magnetic Core Coating Applications. Major Professor: Jing Zhang, Professor.

In transformers used in the electrical industry, a coating, such as magnesium oxide or magnesia (MgO), is needed to coat the magnetic ferrite core, such as silicon steel. The coating is to provide electrical insulation of the layers of the ferrite core material, in order to reduce its heat dissipation loss. The coating also separate the layers of the coiled materials to prevent their sticking or welding during high temperature uses.

The goal of this thesis is to perform a modeling study to understand the mechanical, thermodynamic, magnetic and thermal properties of pure and M-doped (M stands for Mn, Co, or Ni) magnesia, thus providing a theoretical understanding of the application of this group of coating materials for transformer applications.

The study has the following sections. The first section is focused on the mechanical properties of pure magnesia. Using density functional theory (DFT) based calculations, the computed Youngs modulus, Poissons ratio, bulk modulus, and compressibility are 228.80 GPa, 0.2397, 146.52 GPa, and 0.00682, respectively, which are in good agreement with the literature data. Using molecular dynamics (MD) simulations, the computed Youngs modulus is 229 GPa. Using discrete element model (DEM) approach, the bending deformation of magnesia is simulated. Finally, using finite element model (FEM), micro-hardness indentation of magnesia is simulated, and the computed Brinell hardness is 16.1 HB, and Vickers hardness is 16 GPa.

The second section is on the thermodynamic and physical properties of pure and doped magnesia. Using DFT based simulations, the temperature-dependent thermodynamic properties, such as free energy, enthalpy, entropy, heat capacity at constant

volume, and Debye temperature of magnesia, are computed. The X-ray powder diffraction (XRD) spectra of M-doped magnesia are simulated, at the doping level of 1.5%, 3%, 6% and 12%, respectively. The simulated XRD data show that peaks shift to higher angles as the doping level increases.

The third section is on the magnetic properties of pure and doped magnesia. Using DFT based simulations, the calculated magnetic moments increase with the doping level, with Mn as the highest, followed by Co and Ni. This is due to the fact that Mn has more unpaired electrons than Co and Ni.

The fourth section is on the thermal properties of the pure magnesia. Using the Reverse Non-Equilibrium Molecular Dynamics (RNEMD) method, the computed thermal conductivity of magnesia is 34.63 W/m/K, which is in agreement with the literature data of 33.0 W/m/K at 400 K.

1. INTRODUCTION

1.1 Background

In 1882, Lucien Gaulard and John Dixon Gibbs first built and patented a secondary generator, which they designed with an open iron core consisting of a mahogany base and top with four steel rods enclosing a stack of copper disks separated by waxed paper, a linear shape which did not work efficiently as shown in figure 1.1 [1].It was first used in a public exhibition in Italy in 1884 where the transformer stepped down high voltage for use with incandescent light bulbs. In Budapest, Hungary, where Abraham Ganz had emigrated to establish his own steel works factory, designed and built the first wound-core transformer, as shown in figure 1.2 [1]. In 1922 the Shanghai Watson Electric Factory designed and manufactured the first 1.5 kVA power transformer in China [2]. If we were to ask who invented the transformer, we would obtain different answers from different countries [3]. Almost simultaneously, patent applications were submitted by the Hungarians Zipemowsky, Deri and Blthy in 1885, and by William Stanley in 1886, figure 1.3.

George Westinghouse and William Stanley created a transformer that was practical to produce: easy to machine and wind in a square shape, making a core of E shaped plates, and came in both step up and step-down constructions. Although the merit of discovering mutual magnetic induction between two coupled circuits, in 1831, belongs to the great English physicist and chemist Michael Faraday. However, Faraday missed a fundamental feature of transformer, namely, the capacity to transform the generator's voltage and current to adapt them to the load requirements [3, 4].

Since then, there have been series of improvement on transformer's efficiency, particularly toward increasing magnetic flux and minimizing heat loss or core losses.

Fig. 1.1. First patented open core transformer by Gaulard and Gibbs, 1882 [1]

1.1.1 Transformer core losses

The major components in electromagnetic induction applications today are winding and core through which current generates magnetic flux and vice versa. The core is primarily tasked with creation of huge magnetic flux whenever primary winding receives alternating current from the voltage source. However, there are two major losses in transformer core which reduce its efficiency during operation due to eddy current and hysteresis effects as shown in figure 1.5.

Having connected the primary winding to voltage source, the primary current I_p passes through the coil and magnetic field establishes around the coil due to the nature

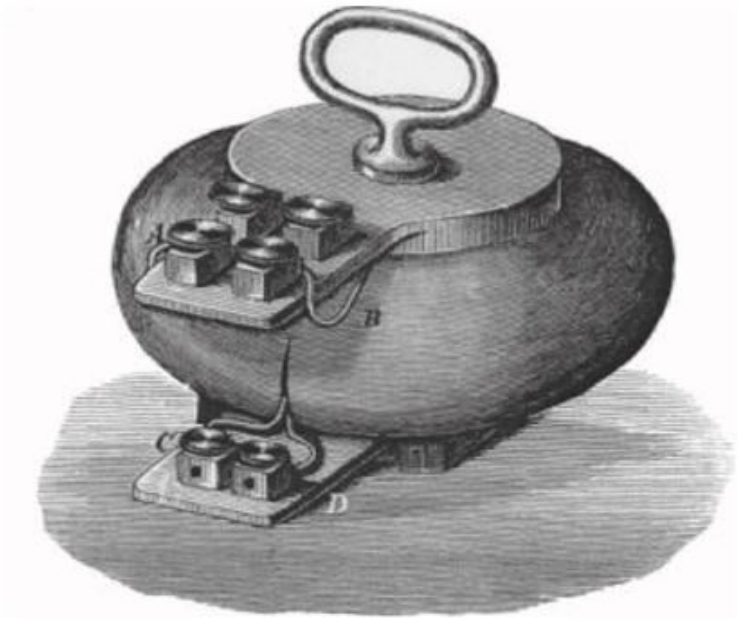

Fig. 1.2. First closed wound core transformer built by the GANZ company in 1884 [1]

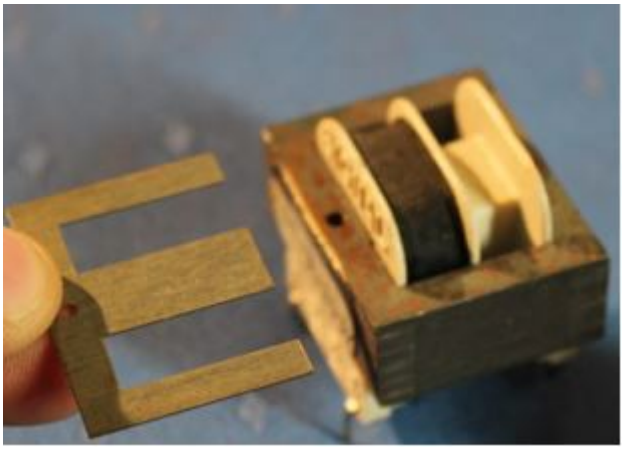

Fig. 1.3. Modern E-core transformer based on Stanley's design [1]

of alternating current. The flux density B(t) is produced in the transformer core and thus resultant magnetic flux $\phi(t)$ varies with time as described in the equation 1.3 [6]

The exciting current

$$i(t) = I_{max} \sin \omega t \tag{1.1}$$

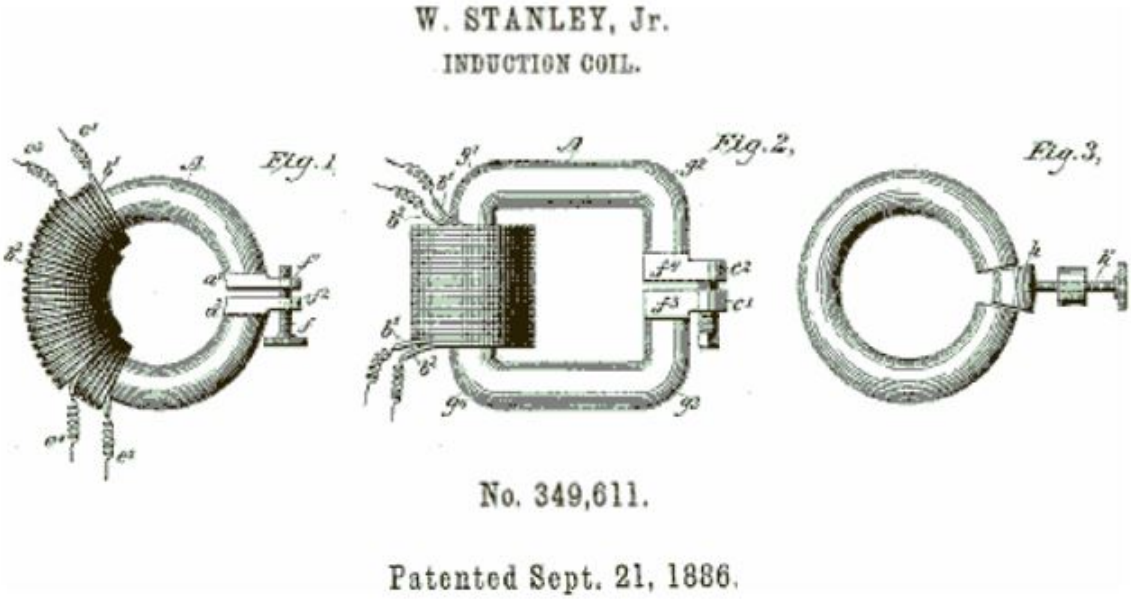
W. STANLEY, Jr.

INDUCTION COIL.

Fig.1.

Fig.2.

Fig.3.

No. 349,611.

Patented Sept. 21, 1886.

Fig. 1.4. William Stanley's patent. In 1900, W. Stanley founded his own company Stanley Electric Manufacturing Co., Pittsfield MA, which was taken over by General Electric in 1903 [1]

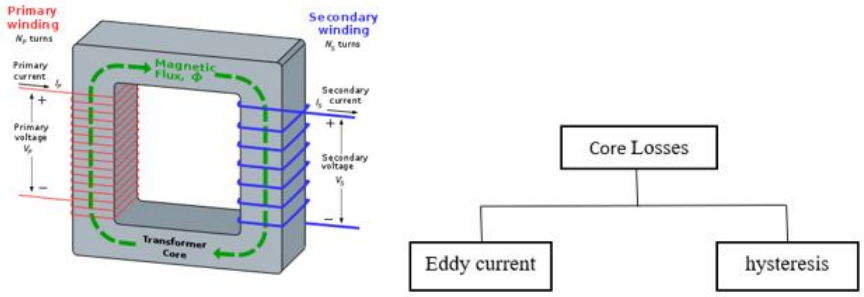

Fig. 1.5. Electromagnetic induction components and core losses [5]

Flux density

$$B(t) = B_{max} \sin \omega t \tag{1.2}$$

Magnetic flux crossing area A

$$\Phi(t) = B(t)A$$

$$\Phi(t) = B_{max}\, A\, sin\omega t$$

$$\Phi(t) = \Phi_{max}\ sin\omega t \tag{1.3}$$

Since magnetic flux is not steady but changes with time, an electromotive force (emf) is induced in the coils which produces eddy current in the transformer core in a certain direction.

1.1.2 Eddy current via solid core

The induced voltage in the coils generates sinusoidal current in the core due to the presence of magnetic flux. Therefore, a circulating current i_{eddy} will result and the direction of i_{eddy} is shown at the instant when B(t) is increasing with time. It is important to note here that to calculate induced voltage in the path, the value of flux to be taken is the flux enclosed by the path of the loop. The magnitude of the eddy current will be limited by the path resistance, R_{path} neglecting other reactance effect. Eddy current will consequently cause power loss in R_{path} and heating of the core [6]. These currents are generated simply because the core is considered a single loop of wire by the magnetic flux as shown in figure 1.6. Since the iron core is a good conductor, the eddy currents induced by a solid iron core will be large. The total eddy current loss in the material will be the power losses of different eddy paths covering the whole cross section.

Induced voltage in the coils, according to faraday's law [7]

$$e(t) = -N\frac{d\Phi(t)}{d(t)}$$

$$e(t) = N\Phi_{max}\omega\cos\omega t$$

$$e(t) = NE_{max}\cos\omega t \tag{1.4}$$

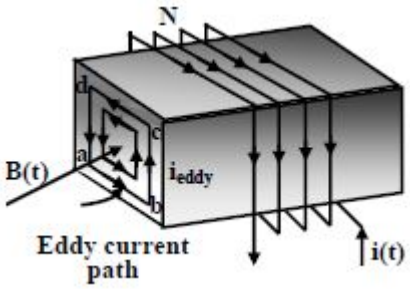

Fig. 1.6. Eddy current path [6]

For N (number of turns) = 1 Root mean square RMS

$$e = \frac{\phi_{max}\omega}{\sqrt{2}}$$

$$e = \sqrt{2}\,\pi\, t\, \Phi_{max} \tag{1.5}$$

where

$$\omega = 2\pi f$$

Also according to Ohm's law, the eddy current loss is

$$P_{eddy} = i_{eddy}^2 R_{path} \tag{1.6}$$

1.1.3 Eddy current via thin plates or laminations for core

It is important to minimize the power loss due to eddy current so that heating of the core is reduced and efficiency of the machine or the apparatus is increased. It is obvious if the cross-sectional area of the eddy path is reduced then eddy voltage induced will be minimized since eddy voltage is proportional to area ($E_{eddy} \propto area$). This can be achieved by replacing solid core with several thin electrically insulated plates (called laminations) stacked together. The idea is shown in the Figure 1.7 while assembling the core, the laminations are kept closely pact. Since current is directly proportional to the material conductivity and resistance is inversely proportional to

the material conductivity (σ). Therefore, we can express power loss due to eddy current as follows

$$P_{eddy} = \sigma_{cd}^2 \times \frac{1}{\sigma_{cd}} \tag{1.7}$$

Therefore, it can be deduced from equation 1.7 that

$$P_{eddy} \propto \sigma_{cd}$$

Hence, we need to reduce the conductivity of the core material in order to minimize eddy current loss. Consequently, silicon is added to steel to reduce it conductivity however, silicon is a weak material and it has 3 to 5% addition limitation to ensure the core strength requirement. Therefore, lamination is the second option to reduce eddy current loss since cross sectional area (A) will be greatly reduced. Resistance is inversely proportional to the cross-sectional area and if resistance is high, the conductivity of material is low and thus eddy power loss

$$R = \rho \frac{l}{A} \tag{1.8}$$

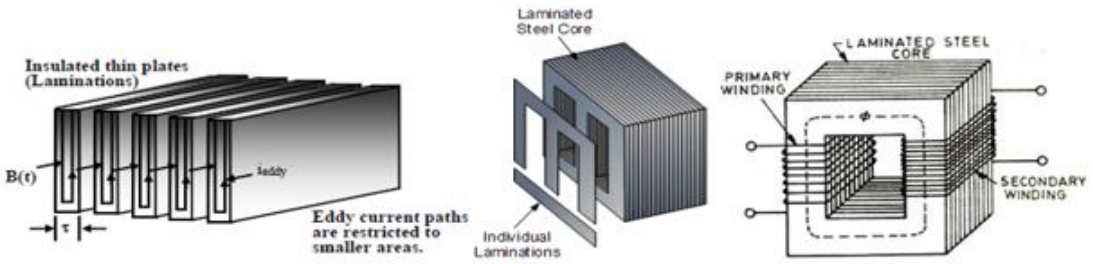

Fig. 1.7. Laminated core to reduce eddy loss [6]

Let area of the loop $ABCD = 2hx$; and volume of the plate $V_{plate} = hL\tau$ according to figure 1.8 Therefore, It follows, from Faraday's law [7], that the magnetic flux crossing the loop is,

$$B_{loop} = B_{max}\, 2hx\, sin\omega t \tag{1.9}$$

$$RMS\,voltage\;\; E = \sqrt{2}\,\pi f B_{max}\,2hx \tag{1.10}$$

Hence, Resistance of the path through which eddy current flows,

$$R_{path} = \frac{\rho(2h+4x)}{L\,dx} \tag{1.11}$$

The expression for the eddy current loss in the plate shall be determined from the power loss in the elemental strip and then integrate suitably to for total loss. Power loss in the loop d_P is given by [6]:

$$d_P = \frac{E^2}{R_{path}} \tag{1.12}$$

$$d_P = \frac{(E^2\,L\,dx)}{\rho\,(2h+4x)} \tag{1.13}$$

$$d_P = \frac{(E^2\,L\,dx)}{\rho\,(2h)} \tag{1.14}$$

since thickness

$$\tau \ll h$$

Therefore, total eddy current loss

$$P_{eddy} = \frac{4\pi^2\,B_{max}^2\tau^2}{\rho}\int_{x=0}^{x=\frac{\tau}{2}} x^2\,dx$$

Eddy loss per unit volume

$$P_{eddy/volume} = \frac{\pi^2\,f^2\,B_{max}^2\,\tau^2}{6\,\rho}P_{eddy} \approx k_e\,f^2\,B_{max}^2\,\tau^2 \tag{1.15}$$

The eddy current loss per unit volume of the material directly proportional to the square of the frequency, flux density and thickness of the plate and inversely proportional to the resistivity of the material. However, the core thickness of the material is the only design variable in core manufacturing and thus, constructed using thin plates called laminations which must be insulated to minimize energy loss due to heating effect. Therefore, the transformer core must be constructed from thin plates closely packed together with refractory materials insulating one from another

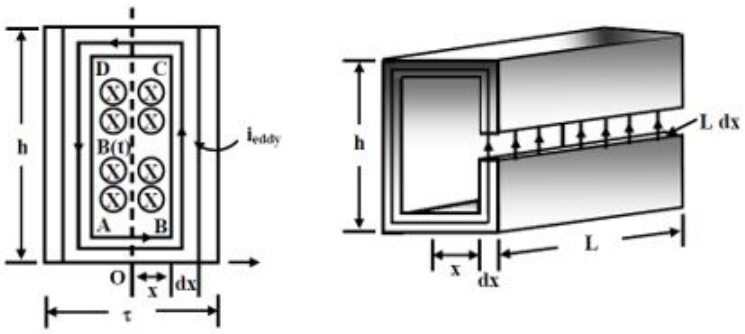

Fig. 1.8. Eddy current path in thin plate [6]

to create separation on each thin limited sheet. This work conducts verification and improvement of mechanical and thermodynamic properties of MgO used in coating process and, as refractory insulating material in transformer core or other electrical devices, the first function of the coating is to provide separation of the various layers as interlamination insulation to give low eddy-current losses and prevent their welding together during high temperature anneals. The second function is the aiding in the chemical purification of the ferrous material to develop the desired optimum magnetic characteristics of such material. The third function of the coating is to form on the surface of the ferrous material a refractory-type coating which will provide electrical insulation between each layer as well as withstand thermal and mechanical stresses developed in the laminations during its use as a core in a transformer or in other electrical apparatus [8, 9].

1.1.4 Hysteresis loss

Due to the nature of alternating current and the magnetic flux set up in the magnetic core of the transformer, the core undergoes a cycle of magnetization and demagnetization through which friction of the molecules against the flow of the magnetic lines of force generated and constantly changing in value and direction due to the influence of the sinusoidal supply voltage. Silicon steel grains oriented in a specific

direction and lost its grain orientation simultaneously. The process generates certain energy loss that leads to lagging of resultant magnetic flux density with increasing magnetic field strength as shown in the hysteresis cycle below and thus reducing transformer efficiency [10]. It can be minimize by using soft iron core or material having least hysteresis loss.

Hysteresis loss per unit volume

$$P_h = K_h f \, B_{max}^n \tag{1.16}$$

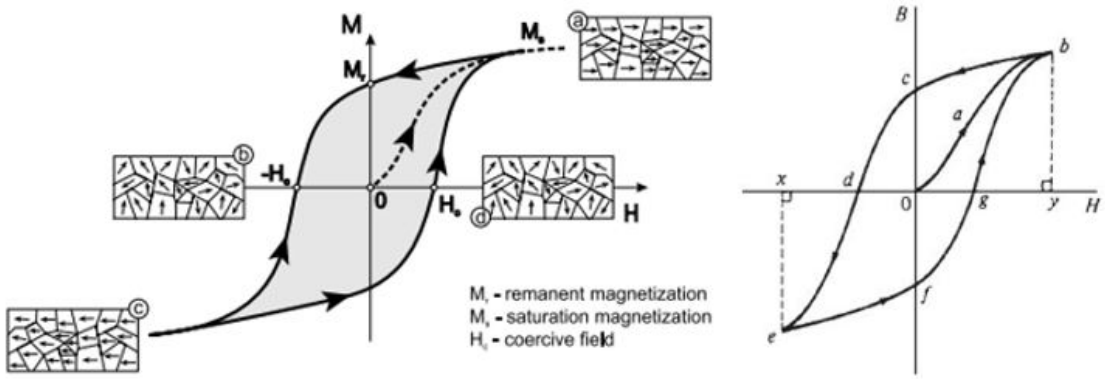

Fig. 1.9. Hysteresis loop [10]

1.2 Literature review

Silicon steel is undoubtedly the most important soft magnetic material in today applications varying from few relays to tons used in generators, motors, and transformers [11]. The economic growth in electrical power generation and high demand of electricity has required development of better steels to decrease wasteful dissipation of energy (as heat) in electrical apparatus and to minimize the physical dimensions of the increasingly powerful equipment [11, 12]. Prior to 1970, the development work was concentrated in the orientation of the (110) [001] direction, toward minimizing the impurity, such as the carbon content and adding silicon up to 3.2%, and in the

gauge reduction to minimize the eddy current loss [13]. Silicon grain-oriented electrical steel was developed in 1945 as a material with a great magnetic property which is used for transformer core of electric devices and machines [13]. Over the few years, there has been increasing demand for electric vehicles (EV) due to global trend of reducing greenhouse gases emissions from fossil fuels, and low-electricity consuming transformers, such as distribution transformer and power transformer, as a result of power efficiency [14]. The role of electrical steel became so important that its contribution to the improvement in the efficiency of the electric motor of EV and other transformer appliances [15]. Therefore, reduction of losses, risk of high operating temperature, energy and costs of transformers cannot be overlooked [16]. A transformer failure ranges from electrical, mechanical or thermal factors which could possibly affect magnetic circuit (Core, yoke and clamp structures), electrical circuit (windings and insulation), or the major components such as core, windings, bushing, solid insulation, tank and so on. The rate of failure of distribution transformers vary in the world, for instance failure rate in India is as higher (12-17%) as compared to developed countries (2-3%) [17]. In Kenya for instance, the failure rate is approximately 10-12% per annum which is far above the failure rate of 2% in the developed countries per annum (as per Kenya Power reported cases of failed transformers) [18]. In the course of building transformers with high electrical efficiency, the laminations of the core need to be electrically insulated, to provide the surface of the magnetic sheet film which functions as interlamination insulation to give low eddy-current losses from one another to ensure the finished core iron losses no higher than measured by an Epstein test.

Furthermore, the design and manufacturing considerations of transformers necessitate the high performance and efficiency as well as reduction of transformer failure rate, by incorporating enabling factors such as grain-oriented approach (figure 1.10) This concept provides optimum electrical and magnetic properties and loss prevention measures by laminating and insulating magnetic cores essentially to provide separation of the various layers and prevent their sticking or welding together during high

temperature anneals. The refractory-type coating which will provide electrical insulation of one layer of ferrous material from the next during its use as a core in a transformer is equally important. Magnesium oxide (MgO) is used extensively as a highly heat resistant separator medium and protective coating in the manufacture of silicon grain-oriented steel by reacting with the silicon steel to form a glass-like film during the high temperature anneal, which acts as an electrical insulator between core laminations in the transformer core [19]. The electrical insulating coating is understood to be derived from coating magnesium oxide on steel, particularly as a protective coating for silicon steel which then forms a film or coating containing Mg SiO yielding an effective electrical insulator when annealed [19]. The core consists of almost half of the total mass of power transformer however, it is not given as much attention - perhaps it accounts for only a small part of the losses - as other components such as winding, bushings, or tap-changers, that make up the transformer. Consequently, the core has only seen little improvements since the first transformers. Nevertheless, the transformer core performs other major functions such as creating magnetic flux circuit between primary winding and secondary winding, support to ensure structural integrity of the whole equipment and therefore it is the heart of the transformer, which would not perform to its full potential if the core is not in perfect condition [20]. In the present technology of the electrical apparatus, the most widely used coating for the ferrous material which is used as the magnetic core is a coating of magnesium oxide and/or magnesium hydroxide by applying it in form of a suspension of magnesium oxide and magnesium hydroxide in water. The insulation thickness on magnetic core can be varied, in order to meet the specific requirement of a given application such as good insulation is required to minimize eddy-current in high frequency applications while insulation is less concerned at low frequency, however required to minimize the effect of eddy-currents during magnetization [21]. The effect of eddy-current creates incomplete magnetization and thus increasing core losses which greatly reduce transformer efficiency.

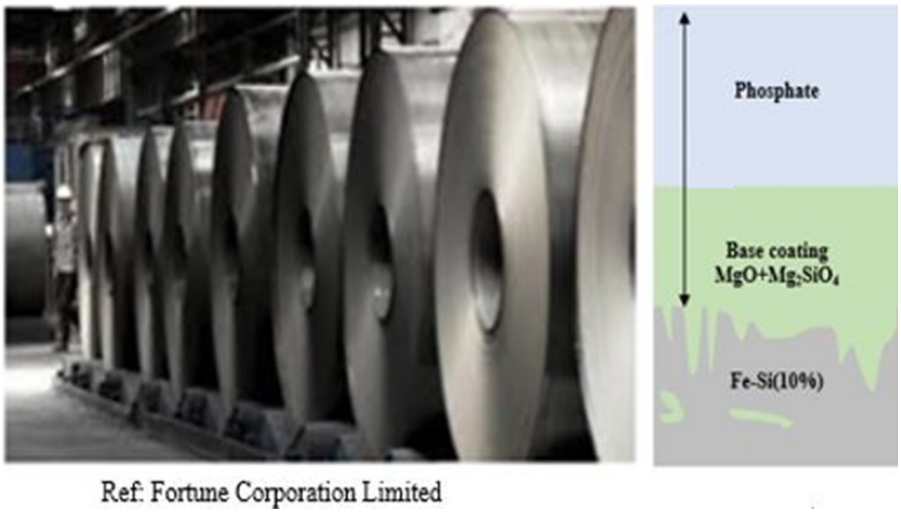

Fig. 1.10. Grain-oriented electrical steel with coating analysis

For an alternating current (AC) magnetic induction applications, ferromagnetic materials must be insulated from each other to create subdivided components that reduce the induction of eddy -currents. Two main factors are the cause of the magnetic deterioration, namely the induced mechanical stress as well as increasing eddy currents due to a damage of the insulation layer between the sheets [22]. MgO is one of the major refractory insulation materials used in the transformer core. The goal of this work is to improve mechanical and thermodynamic properties of MgO through atomistic simulation to ensure effective coating of thin laminated plates of magnetic core. For designing reliable power transformer insulation, electrical stresses, stress duration, stressed volumes, surface stress or creep condition and geometry tolerance must be taken into consideration [1].

1.2.1 Development of electrical steels

The development of electrical steels began when Hadfield published work showing the introduction of silicon or aluminum to steels reduced energy losses by up to four times [23]. Grain oriented steels were invented by Norman P. Goss in 1934 and the process was commercialized by ARMCO, with the first strips being produced in

1939 [23, 24]. Grain oriented electrical steels were produced by many crystal grains oriented in the [001] direction and the (110) planes close to the sheet plane as shown in figure 1.11, through a series of hot and cold rolling. Thereafter, the strip is heated to around 1200 C, stimulating the secondary recrystallisation of these [001] (110) grains, while additive manganese sulphide prevents the growth of other grains to ensure orientated grains and magnetic properties of the steel are improved [23]. Therefore, energy losses are reduced, and steel developed through this process is often referred to as conventional grain oriented (CGO) steel. In 1965 Nippon Steel introduced the production of high permeability (HiB) steels and this process removed one of the cold-rolling stages used in the Goss method with the addition of aluminum nitride as a growth inhibitor [23]. Although, the grains were much larger than those in CGO steels, the hysteresis loss in these steels reduced up to 30-40 %. The phosphate coating applied to the steel was studied in the 1970's with early work indicating that magnetostriction effect was reduced by the coating holding the steel under tension [25].

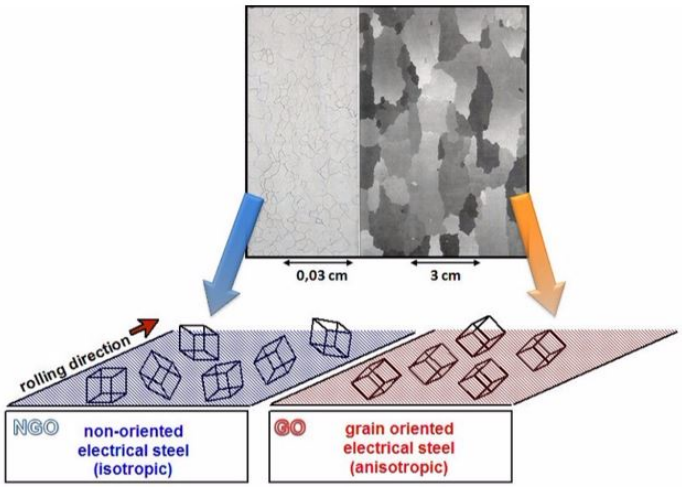

Fig. 1.11. Grain-oriented electrical steel and non-oriented electrical steel [23]

The process diagram of grain-oriented electrical steel at Cogent Power as large coils weighing 20 tons, with a sheet thickness of around 2.5 mm trimmed, passed through

the annealing and de-scaling line, where acid and process known as shot-blasting' removes dirt and scale from the surface is shown in Figure 1.12. Then, the steel undergoes a final cold reduction, where the steel is reduced to its final thickness 0.23-0.3 mm based on customer requirement. After this final reduction, the steel passes through the decarburizing anneal mainly to reduce the amount of carbon within the steel to less than 0.003 % by heating in a mixture of hydrogen, nitrogen and water vapor, as well as other contaminants present to the lower concentrations (such as Sulphur) to ensure less brittleness of the resulting product [23]. At the end of the anneal, the steel is coated in a magnesium oxide slurry, then passes through to the high temperature anneal (HTCA) at 1100 C in hydrogen for five days. This yields the grains grow' to give the typical magnetic properties observed for grain-oriented steels.

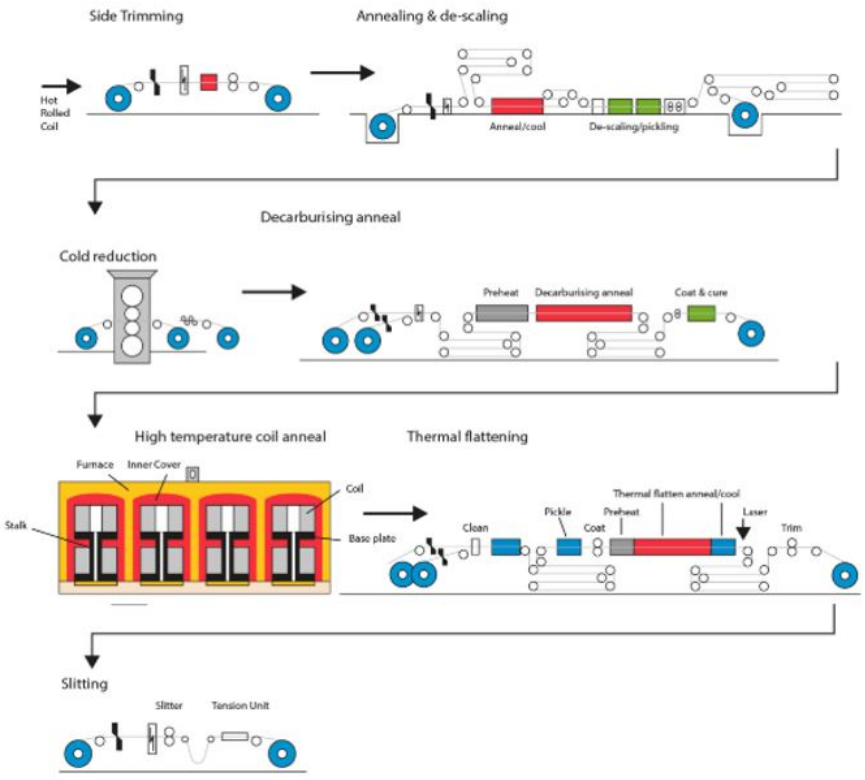

Fig. 1.12. Manufacturing process of grain-oriented electrical steel at Cogent Power Ltd [23]

During this anneal the magnesium slurry reacts with fayalitic (Fe2SiO4) on the steel surface to form forsterite (Mg2SiO4) and is referred to as base coating. Thereafter, the steel sheets pass to the Thermal Flattening line where the final phosphate coating called insulation coating is applied and the steel is heated to 850 C. The flattening effect on the steel and holding it under tension improve its magnetic properties. After the coating has been applied and cured, the steel may be scribed by a laser in order to further improve the magnetic properties by reducing domain size. After this the steels are trimmed to specification and is ready for customer use.

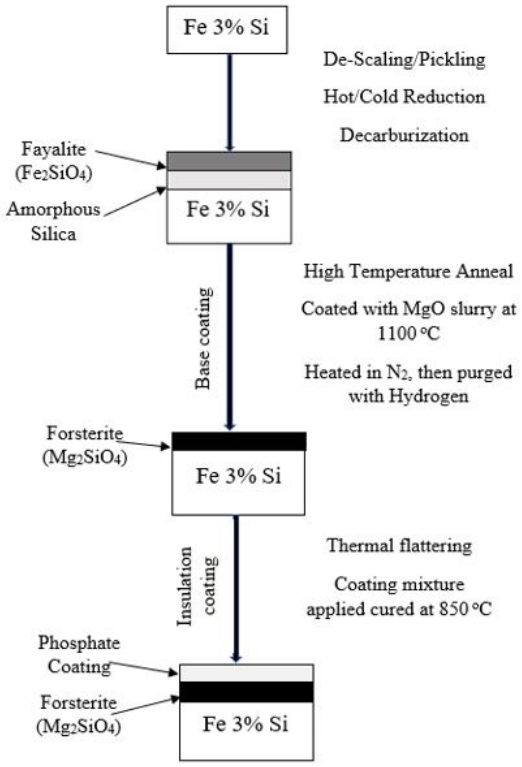

Fig. 1.13. The coatings formed on grain oriented steel during processing a Cogent Power Ltd [23]

1.2.2 Experimental procedures for synthesized MgO

The synthesized MgO comes from chemical reaction of magnesium chloride - $MgCl_2$ and doping element chloride - $MnCl_2$; $CoCl_2$; $NiCl_2$ in the presence of deionized water and respective catalyst [26]. The process is stirred to facilitates

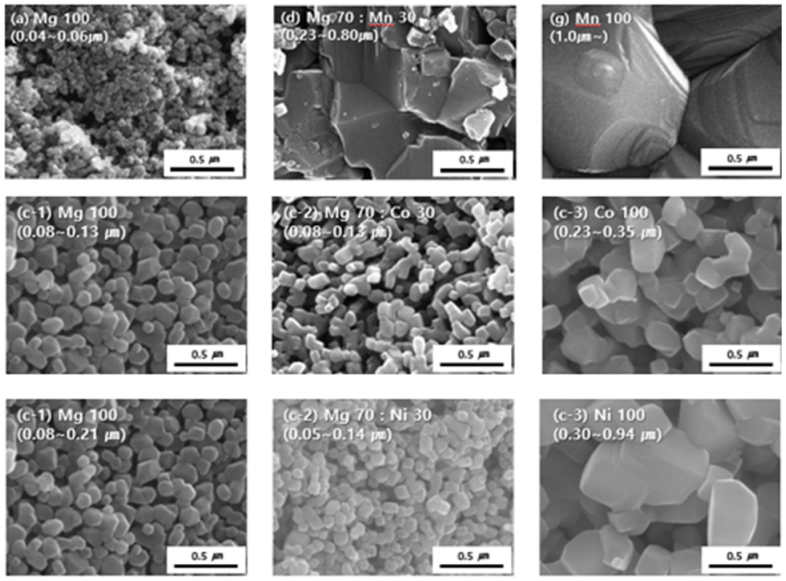

Fig. 1.14. Scanning electron microstructure (SEM) [26]

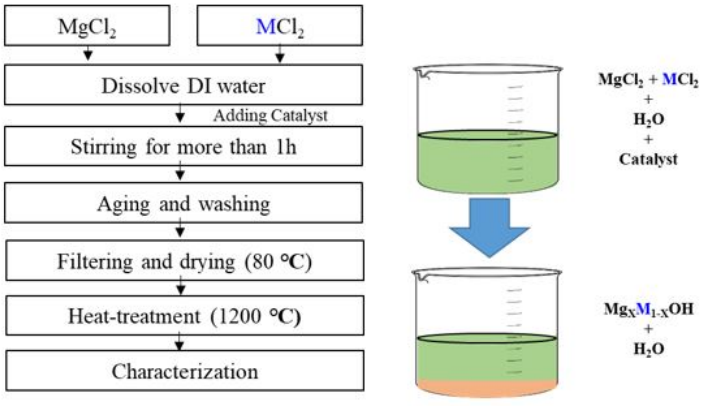

Fig. 1.15. Experimental Procedures for synthesized MgO [26]

reaction for an hour, then passes through aging and washing stage where the product

is established. It is therefore filtered, dried, and heat treated up to 1200^0C as illustrated in figure 1.15 and equation 1.17. Different catalysts such as NaOH; KOH; and NH4OH were applied during this process and each respective product's microstructure was investigated using scanning electron microstructure (SEM) as shown in figure 1.14

$$MgCl_2 + MCl_2 + H_2O \longrightarrow Mg_XM_{1-X}OH + H_2O + HCl \tag{1.17}$$

1.3 Goal and objectives

The economic growth in electrical power generation and high demand of electricity require the development of better magnetic core to decrease wasteful dissipation of energy and to ensure transformer's structural integrity. The refractory coating is widely used to provide electrical insulation without much attention on its magnetic and mechanical properties; leading to transformer's failure incidents in the society. The previous studies have specifically based on density functional theory with little contribution from atomic and particulate perspectives. The goal of this thesis is to simulate magnesium oxide (MgO) single crystal on electronic, atomic, and particulate levels with doping effects of transition elements such as nickel, cobalt, and manganese, in order to establish an improved magnetic and thermomechanical properties of core coating materials, which would increase the overall transformer's efficiency and provide adequate support, and stability for economic growth in electrical generation. To this end, it is critical to understand the fundamental properties and potential failure mechanisms of magnesium oxide. The specific objectives of this work are:

(1) ab initio calculations of mechanical, magnetic, and thermodynamic properties of doped-MgO based on density functional theory.

(2) Atomistic simulation of mechanical properties of magnesia based on molecular dynamics (MD) and finite element method (FEM); and

(3) Particles to particles interaction simulation of mechanical properties of MgO based on discrete element method (DEM).

Achieving the above objectives will help understand the mechanical, magnetic and thermodynamic behaviors of refractory coating materials, thus the failure mechanisms, and improve coating performances.

1.4 Thesis outline

The structure of the thesis is as follows. Chapter 1 provides an introduction to The invention of transformer, basic transformer components, losses in transformer and refractory coating on transformer core. Literature related to the refractory coating materials were also discussed in chapter 1. In chapter 2, the study is mainly focused on the simulation of mechanical properties of magnesium oxide (MgO) through molecular dynamic (MD) simulation, finite element method (FEM), discrete element method (DEM). Chapter 3 aims to develop and compare thermodynamic and physical properties of MgO and doped-MgO. Chapter 4 discusses magnetic properties of MgO and doped-MgO structures using DFT approach. And in chapter 5, the study focuses on thermal properties of MgO. Thereafter, followed by Summary and Recommendations.

2. MECHANICAL PROPERTIES OF MAGNESIUM OXIDE

The mechanical properties of Magnesium oxide (MgO) is studied through molecular dynamic (MD) simulation, finite element method (FEM) using ANSYS, discrete element method (DEM) based on Newton's second law and density functional theory (DFT). The periodic model which allows constant number of atoms, was created with magnesium and oxygen atom interactions of Coulomb-Buckingham potential (during MD simulation) with cut off range 10 under the tensile condition after energy minimization. Bond strength test and thermodynamic properties were investigated based on discrete element method and energy-strain approach through DFT under different small strain patterns. Atomistic interaction of 20% strain at an average temperature of 300 K was also investigated in MD simulation. Hardness test was as well performed based on FEM using Brinell, and Vickers approaches.

2.1 MD computational details

This work was performed by molecular dynamics simulation package. The interatomic potential for MgO atoms is based on the modified embedded atom model (MEAM) using the combination of three terms: (1) the long-range Coulomb potential, where q values are charges for each atom; (2) the Buckingham represents the interaction (a typical electronic repulsion to avoid electron overlapping due to Pauli exclusion principle and an attraction - Van dar Waals energy from dipole-dipole mutually interaction) of two atoms that are not directly bonded as a function of the interatomic distance, where r is the instantaneous position of each atom, while A, ρ and C are constants as given in the table 2.1 and the graphical representation of Coulomb-Buckingham potential used in this simulation is shown in figure 2.1 [27].

$$E = \frac{(Cq_iq_j)}{r} + Ae^{\frac{-r}{\rho}} - \frac{C}{r^6} \tag{2.1}$$

$$where\ \ r < r_c$$

$$r_c = \ cut\ off\ range = 10.0$$

Table 2.1.
Pair coefficient parameters used in this work [27]

Atomic interaction	**Element type**	**Element type**	A(eV)	$\rho(\text{Å}^{-1})$	$C(eV\text{Å}^{-1})$
$Mg^{1.4} - O^{-1.4}$	1	2	9892.357	0.20199	0
$Mg^{1.4} - Mg^{1.4}$	2	2	1309362	0.104	0
$O^{-1.4} - O^{-1.4}$	1	1	2145.735	0.3	30.2222

Molecular dynamics simulation consists of the numerical, step-by-step, solution of the classical equations of motion, which for a simple atomic system may be written [28].

$$f_i = m_i\ddot{r}_i \tag{2.2}$$

$$f_i = -\frac{\partial}{\partial x}U_i \tag{2.3}$$

The atomistic simulations are based on a classical Born description of the lattice with pair potentials acting between atomic species. The ionic interactions consist of two components: a long-range Coulombic interaction which are evaluated both in real and in reciprocal space according to the Ewald's method [30] and a short-range interaction, which accounts for the effect of electron cloud overlap and Van der Waals energies. In this study short-range terms are approximated using parameterized pair potentials of the Buckingham form where A, and C are the potential parameters as stated in table 2.1. Table 2.2 shows lattice parameters of unrelaxed crystal while table 2.3 shows the comparison of experimental and computational values.

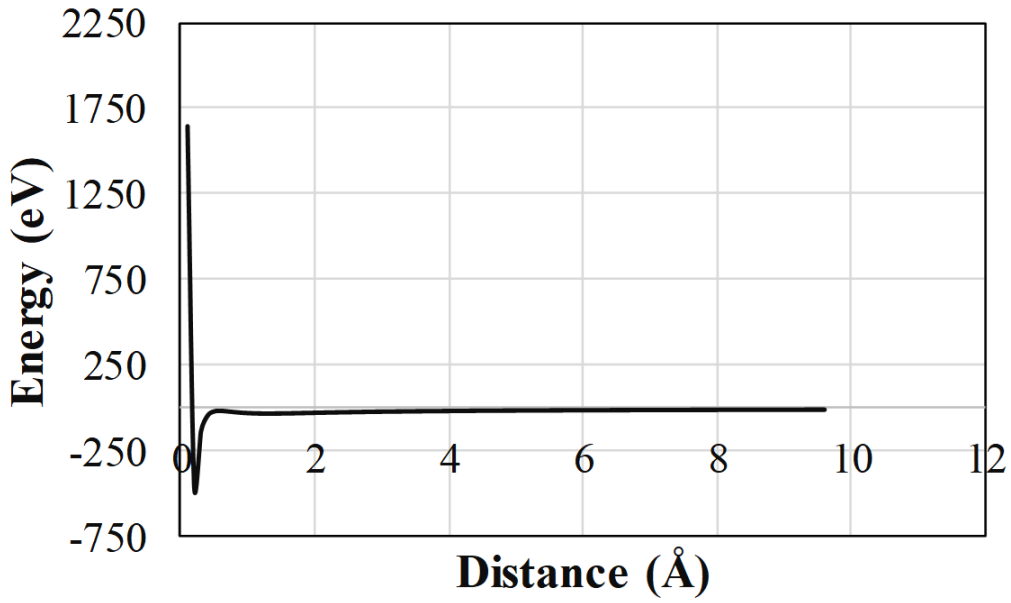

Fig. 2.1. The Coulomb-Buckingham potential curve used in this work [27, 29]

Table 2.2.
Lattice parameters of the original unrelaxed crystal [31]

Temp (K)	**a(Å)**	**b(Å)**	**c(Å)**	$\alpha(^\circ)$	$\beta(^\circ)$	$\gamma(^\circ)$
298	4.21154	4.21154	4.21154	90	90	90
0	4.20565	4.20565	4.20565	90	90	90

2.1.1 Simulation procedure

The simulation was done using the molecular dynamics package with $16.8448 \times 4.2112 \times 4.2112$ Å^3 atomistic model. The atomistic model was created in MD environment as a periodic simulation box. The interaction among atoms was defined by the combined Coulomb-Buckingham long-range potential, with a cut off distance of 10 $\dot{A}$. The original box was first subjected to energy minimization at a room temperature of (298 K) for 100 ps, and strain steps based on energy-strain approach was then

Table 2.3.
Lattice constants comparison with experimental and computational results in literature [32]

Lattice constant	This work	Calculation [32]	Experimental [32]	Angle
a(Å)	4.2112	4.2170	4.2394	$\alpha(^\circ) = 90$
b(Å)	4.2112	4.2170	4.2394	$\beta(^\circ) = 90$
c(Å)	4.2112	4.2170	4.2394	$\gamma(^\circ) = 90$

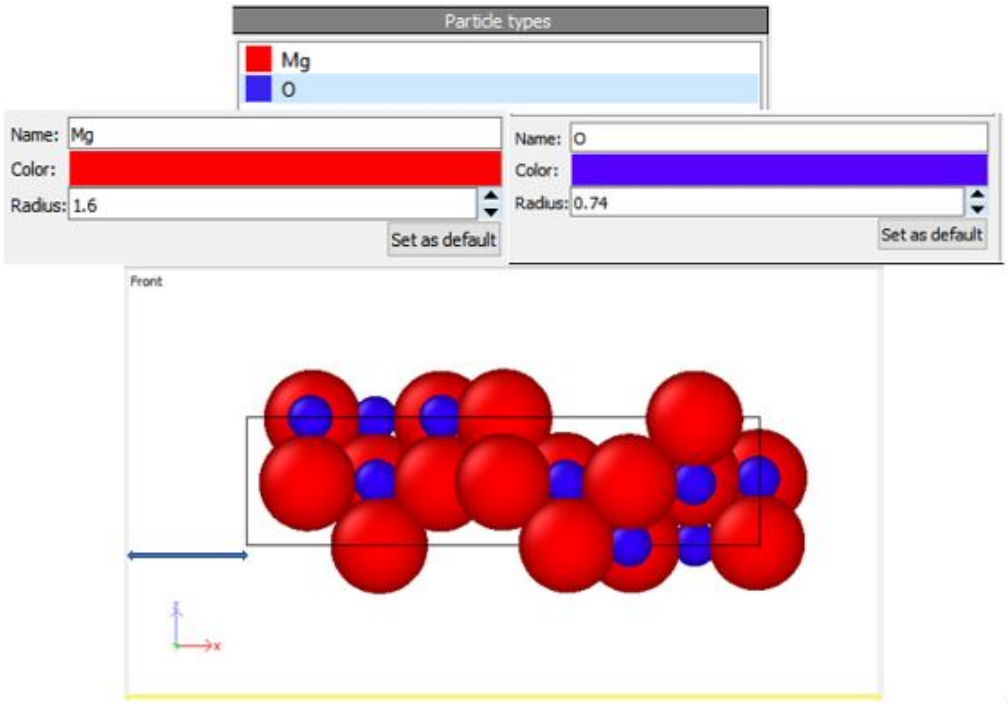

Fig. 2.2. Initial molecular dynamics model for uniaxial tensile test simulation

applied along horizontal direction until strain of 0.2 with the temperature maintained at 300 K based on NPT ensemble. The time step was set to 0.001 ps. During the simulation, the average energy, including total energy, potential energy, and kinetic energy and the average stress were calculated for each 100-time step. The initial and

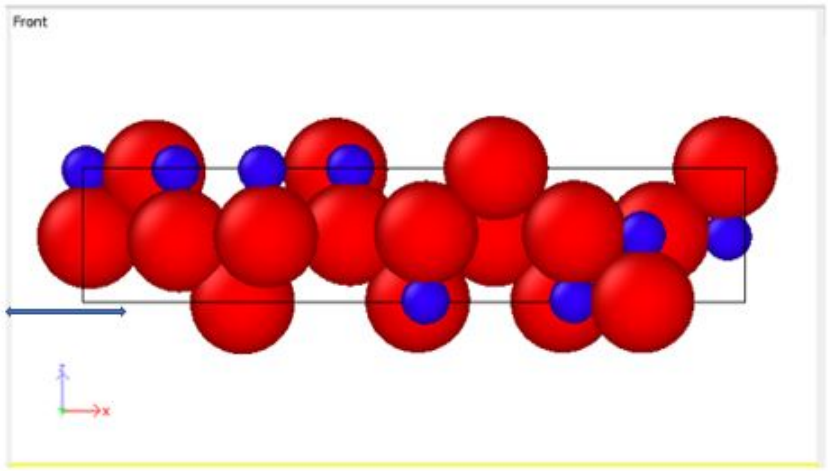

Fig. 2.3. Final molecular dynamics model for uniaxial tensile test simulation

final molecular dynamic models based on stress-strain approach are shown in figure 2.2 and figure 2.3

2.2 Density functional theory and simulation detail

Density functional theory (DFT) method was used to investigate thermodynamic properties and elastic constants of MgO using DFT code based on Schrodinger equation (energy level of the wave function of electron). The local density approximation was applied from exchange correlation setting and norm-conserving pseudopotential was applied in the reciprocal space with k-point mesh of $6 \times 6 \times 6$. Energy cutoff was set to 340 eV with fine self-consistent field (SCF) tolerance, and calculation was based on density functional theory with Generalized Gradient Approximation (GGA) in the scheme of Perdew-Burke-Eruzer (PBE). GGA functionals are selected because they are more reliable than LDA functionals for predicting transition metal systems. The initial structure was first optimized to minimize the energy and ensure more accurate results; thus, the phonon calculation was conducted based on 29 phonon vectors generated and thermodynamic properties and elastic constants were calcu-

lated using the optimized model by applying 6 strain steps based on energy-strain approach according to Schrödinger equation

The Schrödinger equation

$$E\psi(x) = -\frac{\hbar^2}{2m}\frac{d^2\psi(x)}{dx^2} + V\psi(x) \tag{2.4}$$

2.3 Model and simulation of Vicker's indentation via FEM

According to Vicker, the hardness H_v of a material is the ratio between the load applied to the indenter, F, and the indentation surface area A [33].

$$H_v = \frac{2F\sin\theta/2}{d^2} \tag{2.5}$$

$$d = 2a\sqrt{2} \tag{2.6}$$

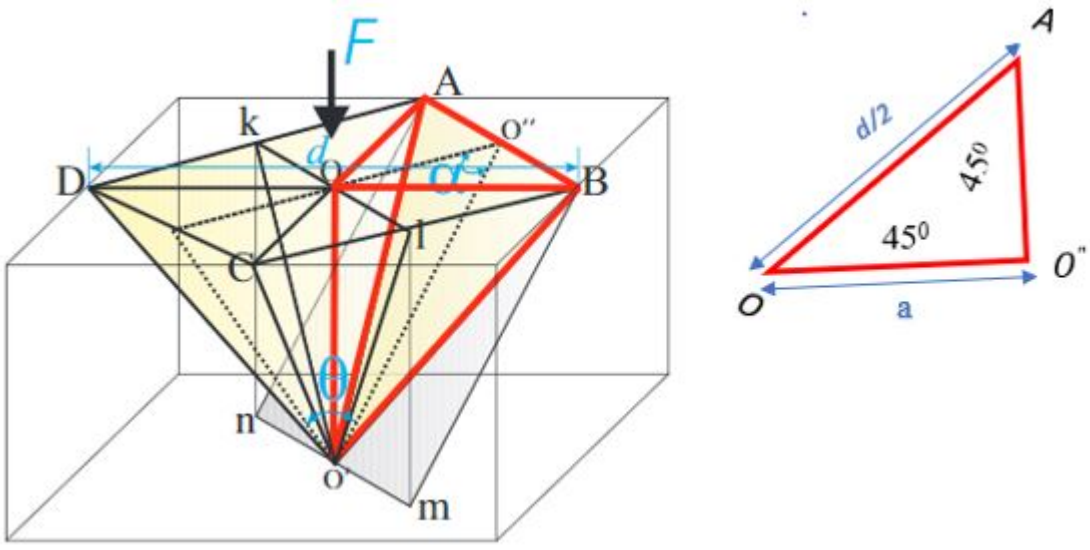

Fig. 2.4. Squared diamond pyramid indenter illustration. The red framework highlights one of four triangular based pyramid indenters [33]

where d and θ are mean diagonal of impression and angle between opposite faces of the diamond squared pyramid indenter, respectively as shown in figure 2.4. In order

to derive our model, we assume that the diamond squared pyramid indenter can be divided into four triangular based pyramid indenters and that the Vicker's hardness is measured within the elastic scale [33]. Also, shear modulus G which specifies the ratio between shear stress and the shear stain can be defined as

$$G = \frac{F}{4A \tan \propto} \tag{2.7}$$

With the assumption of shear elastic deformation, the shear area klO' as shown in figure 2.4 can be approximated as follows [33]

$$A = \frac{1}{8} d^2 \tan \propto \tag{2.8}$$

Therefore,

$$G = \frac{2F}{d^2 \tan^2 \propto} \tag{2.9}$$

Combining equations 2.5 and equation 2.9, the Vicker's hardness becomes

$$H_v = G \tan^2 \propto \sin \theta/2 \tag{2.10}$$

For Vicker squared based pyramid indenter, the followings conditions are assumed,

$$\theta = 136^0$$
$$\propto = \frac{\pi - \theta}{2}$$

Hence,

$$H_v = 0.151G \tag{2.11}$$

Equation 2.11 describes a theoretical evidence of the linear correlation behavior observed by Teter [13], as reflected by the data shown in figure 2.5

2.3.1 Simulation procedures

There are three material properties in this work to build the models. 2-D 8-node planar element PLANE183 is used to model all the areas of indenter, substrate,

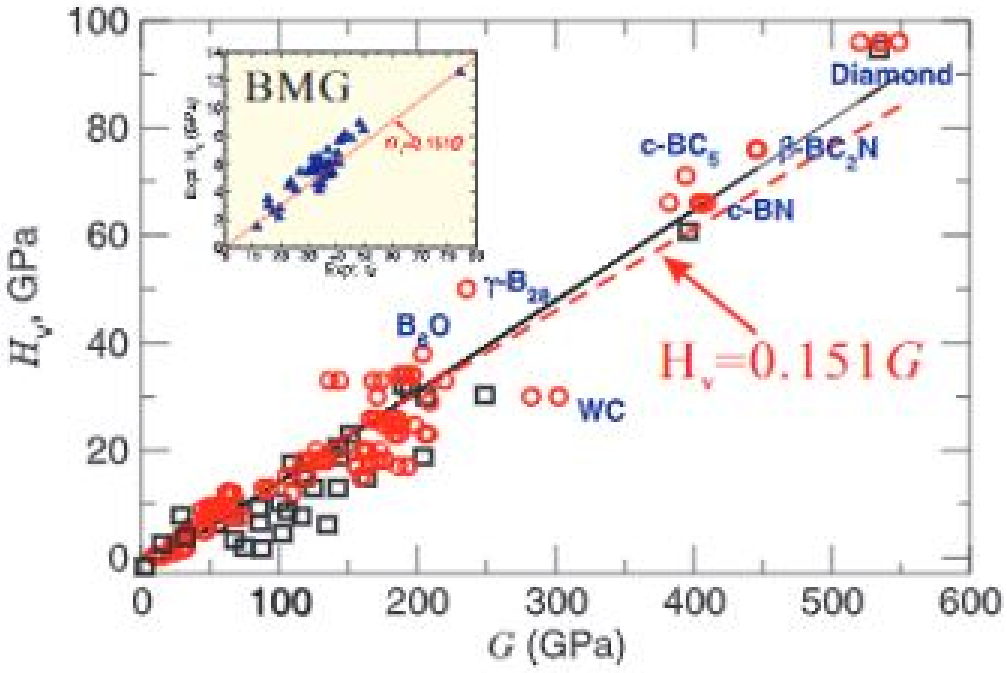

Fig. 2.5. Correlation of experimental Vickers hardness (Hv)with (a) bulk modulus (B) and with (b) shear modulus (G) for 39 compounds [34,35]. The solid line denotes empirical Teeter's fitting values, whereas dashed lines correspond to the value derived from Eq. 2.11 Simulation procedures

and bulk materials. This element type is chosen due to its axisymmetric modeling function, linear isotropic and bilinear isotropic material properties were defined in substrate material to ensure large deflection and large strain. The 2-D Vicker's indenter was formed from AO'O" triangular shape from figure 2.4 and the relationship to establish mean diagonal diameter is shown in equation 16. A contact pair consists of CONTACT123 and TARGET123 elements was defined with contact element TARGET123 employed at the indenter surface while contact element CONTACT123 is used at the upper surface of substrate. The bottom indenter surface and the thin film top surface of substrate formed a contact pair. The boundary conditions are met by applying all nodes on the y axis to only have the displacement in y direction while the x direction displacement is set to zero and the bulk material base is constrained

by fixed boundary conditions. All the nodes on the base cannot move in any direction and the material properties for MgO used in simulation is shown in table 2.4.

Table 2.4.
Material properties used in FEM simulation

Property	**Value**
Young's modulus	250 GPa
Density	3.58 g/cm^3
Poisson's ratio	0.231
Bulk modulus	280 GPa

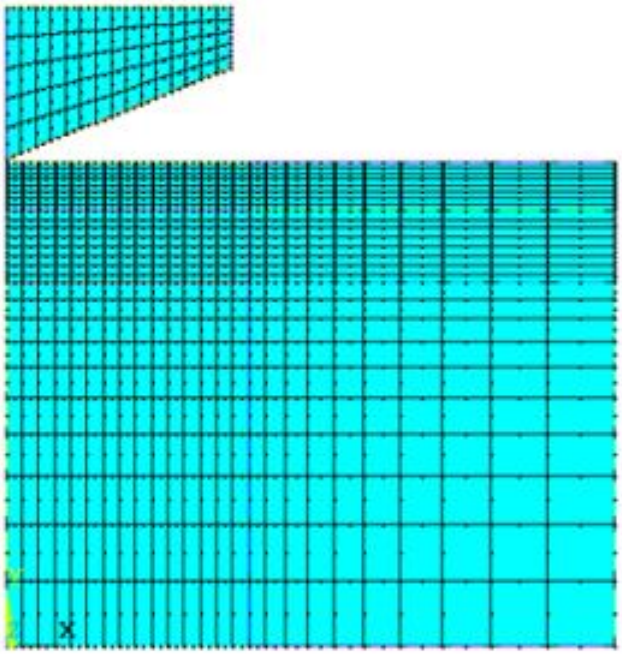

Fig. 2.6. Meshing density illustration

There are 4 different meshing density zones present with contact area has the finest mesh as shown figure 2.6. All the nodes on the upper surface of the indenter are coupled together to ensure that those nodes have the same y displacement. There

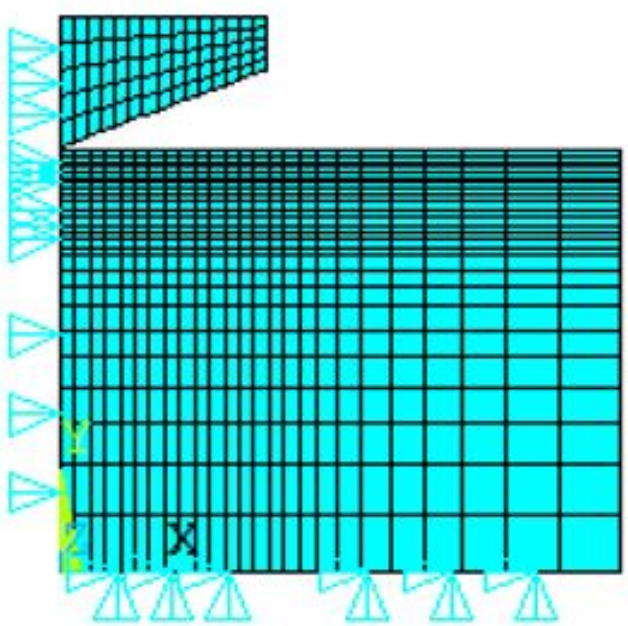

Fig. 2.7. Boundary condition illustration

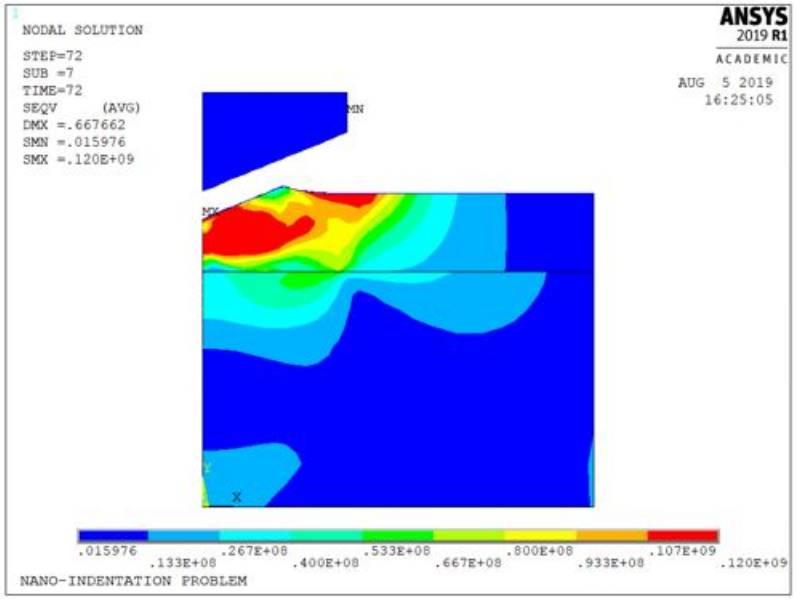

Fig. 2.8. The von Mises stress (Pa) distribution in model

are 72 load steps used in the models which consists of loading and unloading. The loading ranges from 1 to 36 load steps and unloading were from 37 to 72 load steps.

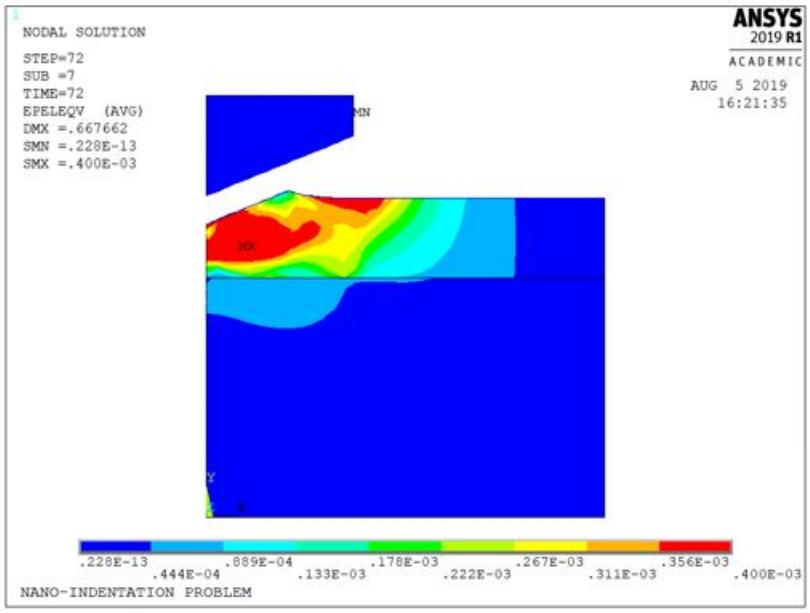

Fig. 2.9. Elastic strain distribution in model

The indentation behavior is simulated by increasing the indenter displacement in small increments in negative y - direction up to the maximum indentation depth. During the unloading step, the indenter returns to its original position incrementally from 37 to 72 load steps.

2.4 Model and simulation of Brinell indentation via FEM

Another hardness test simulated in this work is Brinell's test. The Brinell hardness number (HB) is proportional to the test force divided by the surface area of the indentation [36]. Hardness, as applied to most materials, has been in use for many years to evaluate material property by revealing its values and importance which cannot be overlooked. The information from the test can complement other tests such as tensile test, compressive test, fracture test or impact test to provide critical performance information.

Ideally, Brinell indenters are ball-based modeled with an angle of 360^0 which is assumed to be isotropic. Due to experimental purpose, the computational analysis

would be performed on the whole geometry and due to pair contact effect, the tip of the modeled indenter is thus assumed to initially contact with substrate. The MgO sample block is 13 mm by 13 mm and 12 mm in thickness while indenter is modeled as ball with radius of 2.5 mm.

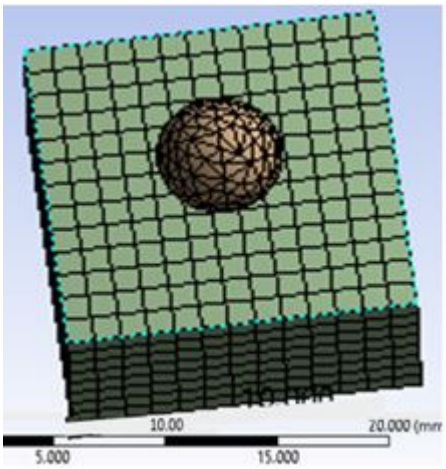

Fig. 2.10. Geometry of the Brinell indentation meshed model

2.4.1 Brinell's hardness test procedures

BHN' is Brinell Hardness Number is calculated as thus [37]

$$BHN = \frac{2P}{\pi D(D - \sqrt{D^2 - d^2}} \tag{2.12}$$

where

P' is applied load in kg,

D' is diameter of ball in mm,

d' is diameter of indentation in mm,

t' is depth of the impression in mm,

During the experiment, the full load was applied for 10 to 15 seconds and the two perpendicular diameters of the indentation left in the surface of the material after removal of the load were measured and the average was calculated. The surface area

of the indentation was calculated. The force condition is assumed distributed load over a surface boundary and thus calculating the stress as following [37].

Loading

$$\sigma = \frac{F_{load}}{A} \tag{2.13}$$

holding

$$\sigma = \frac{F_{max}}{A} \tag{2.14}$$

unloading

$$\sigma = \frac{F_{load}}{A} \tag{2.15}$$

Where:

A is the surface area of the indentation and F_{load} and F_{unload} are defined as

$$F_{load} = F \times t \tag{2.16}$$

$$F_{max} = F \times t_{load} \tag{2.17}$$

$$F_{unload} = F \times *(t_{tot} - t) \tag{2.18}$$

$$t_{tot} = t_{load} + t_{unload} + t_{hold} \tag{2.19}$$

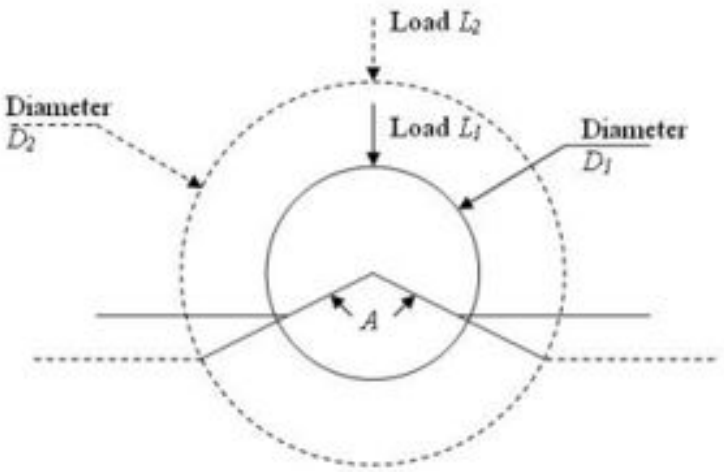

Fig. 2.11. Load - diameter constant ratio illustration [38]

$$\frac{L_1}{D_1} = \frac{L_2}{D_2} = Constant \tag{2.20}$$

$\dot{F}$ is the loading rate and t_{tot} is the total time of the whole period. In general, one should not attempt to determine a Brinell hardness number if the diameter of the indentation is smaller than 2.4 mm (24%) or larger than 6 mm (60% of a 10 mm diameter ball). One of the most useful features of Brinell hardness test derives from the observation is that if the ratio of Force F (in kg) to the square of Ball Diameter D (in mm) is kept constant, one can obtain an approximation of the same BHN (Brinell Hardness Number) as measured with the standard parameters [38].

2.4.2 Domain discretization and simulation details

To make the Brinells indentation model computationally feasible, a relatively medium mesh is defined for both indenter and the substrate with adaptive mesh option selected. Then, body mesh was created between the slave and master bodies, as shown in figure 2.10, to establish a more refined mesh in order to ensure more accuracy during the indentation process. The concept was that the indenter is pressed into the test sample under the assumption of both minor load (when the equilibrium has been reached) and the major load (force which is applied additionally to the minor load) are converted, in the form of equation 2.21 to initial velocity (v_{in}) which drives indenter into the substrate resulting to the increase in penetration. After the equilibrium has been reached again, the major load is removed while the minor load is kept. In this study, velocity (10 m/s) was applied to the indenter and the reaction force generated between the indenter and substrate yields the stress - strain curve.

Force to velocity conversion equation, assumed air resistance is negligible

$$F \times d = m \times g \times d = \frac{1}{2} m \times v_{in}^2 \tag{2.21}$$

Where d is the falling height distance, g is acceleration due to gravity, v_{in} is initial velocity, F is the load. The deformation distribution and equivalent stress distribution are shown in figure 2.12 and 2.13 accordingly.

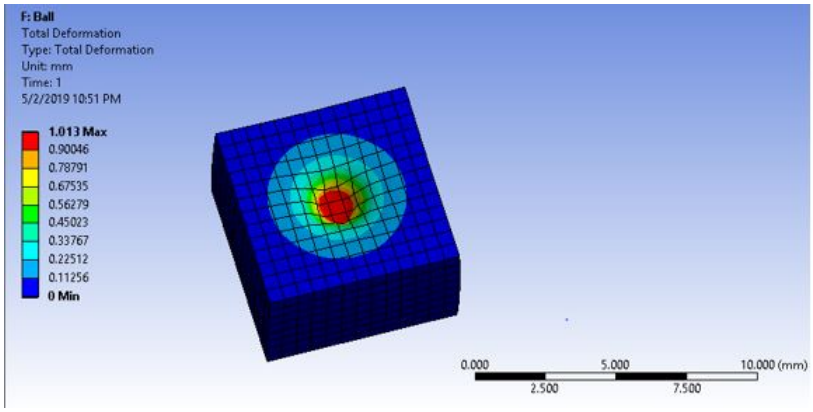

Fig. 2.12. Deformation distribution (Indentation)

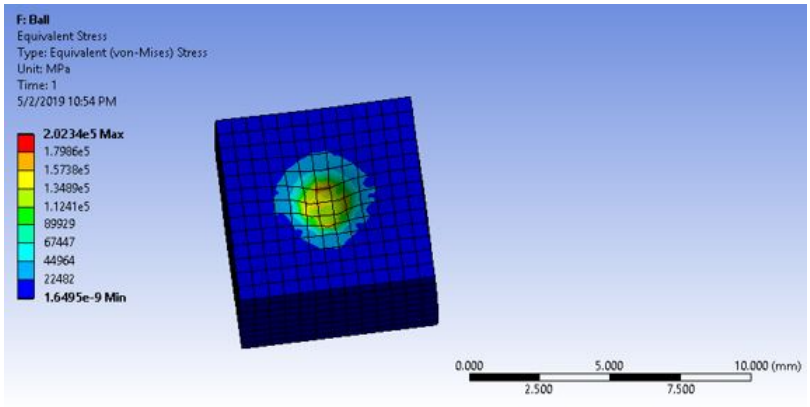

Fig. 2.13. Equivalent stress distribution (Indentation)

2.5 Discrete element method (DEM) model and simulation detail

The Discrete element method (DEM) which was first proposed by Cundall and Strack (1979) has become a standard numerical simulation methodology for modelers dealing with all kinds of particulates and this method (DEM) has proved to be an effective method in modelling rock-like materials [39, 40]. The nature of DEM makes it suitable for dealing with optimization' in uniaxial compression simulation, with consideration of friction coefficient as a factor governing the shear strength and dilation angle, and to calculate an optimum set of microparameters used in generat-

ing models to be tested [41, 42]. Numerical modelling generates a new approach to better understand material property relations by systematically changing individual input parameters while keeping all other parameters constant. Many tests have been conducted through the discrete element method such as shear test, heat transfer test, stress - strain test, or energy - based test [43]. The mechanical behavior of the model material is not predefined, as in continuum approaches during the simulation, but emerges from the interaction of particles [44].

2.5.1 Simulation detail

The simulation was performed by discrete element modeling software (DEM). The bulk material as magnesium oxide (MgO) in the DEM creator tree and material interactions based on bond formation principles with contact radius was defined accordingly. The equipment material was stated as steel with material interaction properties set to default in term of coefficient of restitution, coefficient of static friction, and coefficient of rolling friction. Then, box geometry with (0 0 50) and (200 50 100) in x y z coordinates and loading plane with a linear translation kinematic in z-direction at 0.13 m/s and factory particle, set to static mode of 1E-12 seconds start time and maximum attempts to place particles, were created. The particle to particle bonding physics interaction with critical normal stress, critical shear stress, normal stiffness per unit area, and shear stiffness per unit area are predefined in the creator tree before the beginning of simulation.

The simulation is analogous to compressive spring with two ends represent the centers of atoms being simulated. The contact particles are bonded together by the bonds, which can resist normal force, shear force and bending moment between particle p and particle q that are in contact with each other. The X_p and X_q are their coordinates of the two atoms respectively and dir_{pq} and dir_{qp} are the vectors pointing from their centers to the contact point A respectively. Also, the vector dir_{pq} and vector dir_{qp} rotate within θ_p and θ_q respectively at a specific time. The contact

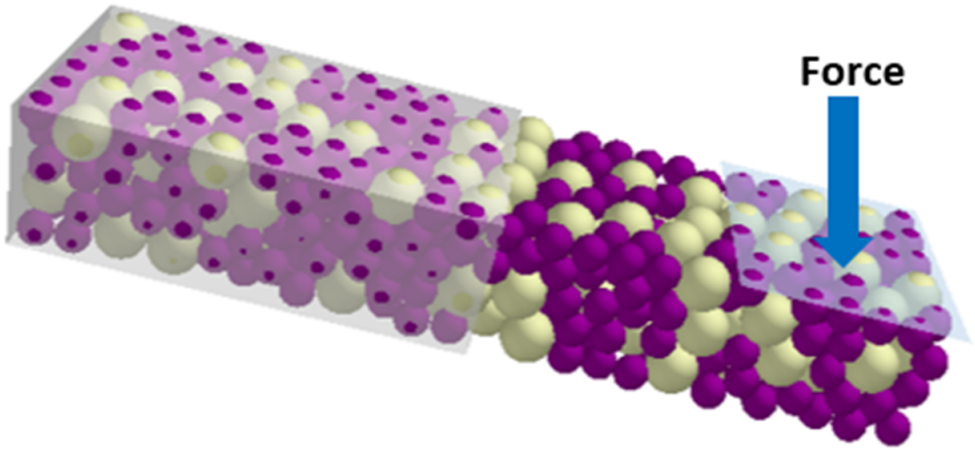

Fig. 2.14. Random particle to particle interactions of MgO illustration

forces and moment applied to particle p from particle q through the bond are normal force F_{pq}^{nr}, shear force F_{pq}^{tn} and moment M_{pq} as shown in figure 2.15 and particle to particle interaction model is shown in figure 2.14.

The constitutive equations of force according to newton's second law and moment on bond strength govern the simulation are [45]

$$m_i \ddot{x}_i = m_i g + \sum\nolimits_j F_{ij} \tag{2.22}$$

$$I_i \ddot{\theta} = \sum\nolimits_j (r_{ij} * F_{ij}) \tag{2.23}$$

Hence, it can be redefined as following since gravity effect is assumed negligible during the simulation

$$F_{pq}^{tn} = -k_s \varepsilon_{pq}^{s} \tag{2.24}$$

$$M_{pq} = -k_m(\theta_p - \theta_q) \tag{2.25}$$

Where k_s and k_m are shear stiffness and bending stiffness accordingly, dis_{pq} is the original distance between p and q, while ε_{pq} is shear strain of the bond between p and q which is the ratio of deformation in tangential direction to dis_{pq}. A nonlinear

stiffness model to describe the relationship between normal force and normal strain undergoing tension and the force in normal direction is expressed as [45]

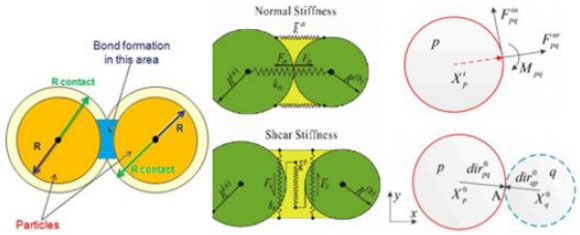

Fig. 2.15. Bonded particle model [45]

if $\varepsilon_{pq}^{n} > 0$

$$F_{pq}^{nr} = k_n \varepsilon_0^n (1 - \exp(-\varepsilon_{pq}^{n} / b\varepsilon_0^n) \tag{2.26}$$

but if $\varepsilon_{pq}^{n} \leq 0$

$$F_{pq}^{nr} = k_n \varepsilon_{pq}^{n} \tag{2.27}$$

where b is shape coefficient of the nonlinear elastic model and ε_0^n is the ultimate normal tensile strain and ε_{pq}^{n} is expressed as [45]

$$\varepsilon_{pq}^{n} = \frac{dis_{pq}^{t} - dis_{pq}^{0}}{dis_{pq}^{0}} \tag{2.28}$$

If the bond is broken or no bond exists between particles p and q which are in

Table 2.5.
Bond category of MgO through DEM simulation

DEM Bond simulation categorization	**Force range (KN)**
Low Category	0 - 54.8
Medium Category	54.8 - 218
High Category	218 - 275

contact with each other, then only normal force and shear force exist between them.

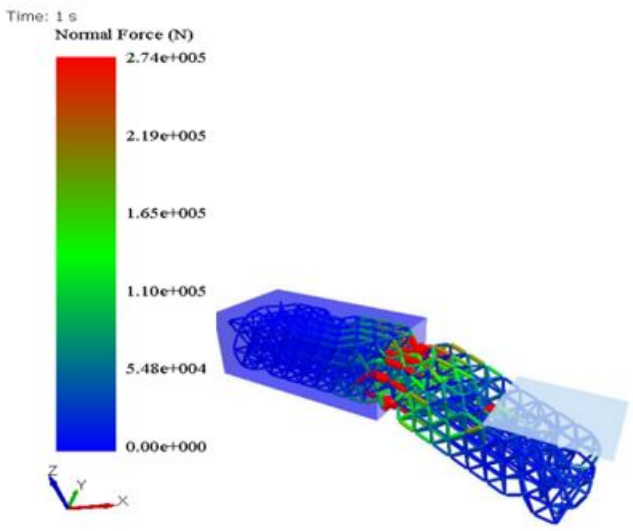

Fig. 2.16. Bond stress analysis of MgO through DEM simulation

The normal force F_{pq}^{nr} is calculated by equations (2.26), (2.27) and (2.28), dis_{pq}^{0} in equation (2.28) should be replaced by the sum of the radii of p and q. The shear force is determined from [45]

$$F_{pq}^{tn} = \mu F_{pq}^{nr} \tag{2.29}$$

and compressive force F_c and compressive strength σ_c are defined as follow

$$F_c = -F_{pq}^{nr} \tag{2.30}$$

$$\sigma_c = -\frac{F_{pq}^{nr}}{A} \tag{2.31}$$

$$U = \int_{x1}^{x2} F_{pq}^{nr} x \, dx \tag{2.32}$$

The intact and broken bonds of MgO as shown in figure 2.16 experience certain magnitude of stress at every time step during the simulation. The maximum and minimum applied loads are 0 KN and 274 KN which is large enough to create bond reaction categorized into low, medium and high reactive bonds as summarized in the table 2.5 within 1s period. However, the applied force proves agreement with literature result of compressive strength: 2200 - 2600 MPa [46, 47]

2.6 Results and discussion

2.6.1 Atomistic result of MD simulation

Figure 2.2 and figure 2.3 shows initial molecular dynamics model and the final molecular dynamics model configurations of MD uniaxial tensile test simulation. Figure 2.3 shows the 20% strained model in X-direction and the periodic boundary condition allows the replacement of outgoing atoms directly from opposite sides as this is required to maintain constant number of atoms in the simulation box. The stress - strain curve was plotted from atomistic perspective and young's modulus was calculated based on line fitting technique from figure 2.17. Although, the accuracy of atomistic simulation largely depends on the potential, however, young's modulus (E $\approx$ 229 GPa)and poisson's ratio ($\nu_{xy} = 0.2397$)were relatively in good agreement with our simulation from DFT results and literature as shown in table 2.6.

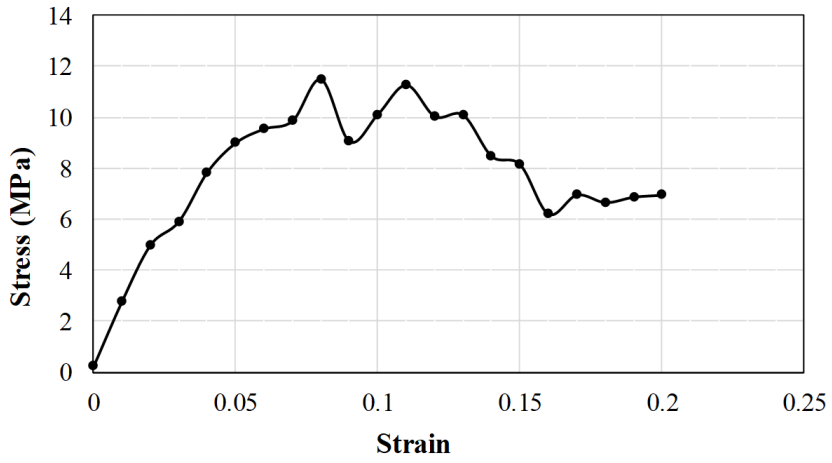

Fig. 2.17. MgO - atomistic tensile test curve

Table 2.6.
Young's modulus, poisson's ratio, bulk modulus, compressibility and comparison with reference data

Properties	**This work**	**Ref. [48]**	**Ref. [49]**
Young's modulus (GPa)	228.80 (X, Y and Z-axes)	227.58	249
Poisson's ratio	$\nu_{xy} = 0.2397$ $\nu_{xz} = 0.2397$ $\nu_{zx} = 0.2397$ $\nu_{yx} = 0.2397$ $\nu_{yz} = 0.2397$ $\nu_{zy} = 0.2397$	0.23414	0.18
Bulk modulus (GPa)	146.52 +/- 0.436	142.67	155
Compressibility (1/GPa)	0.00682	n/a	n/a

2.6.2 DFT result and discussion

With energy - strain approach, elastic constants can be obtained by analyzing energies under different small strain patterns DFT. A finite strain amplitude is specified for each strain pattern. Once elastic constants are determined, young's modulus and poisson's ratio can be deduced [50]. Elastic constants were calculated by applying 6 strain steps with each step of 0.003. The calculated elastic stiffness constants, elastic compliance constant as well as the bulk modulus, young's modulus and poisson's ratio were calculated based on optimized model with our results relatively agree with the literature data as shown in table 2.6 and table 2.7 [48, 49, 51, 52]

By using molecular dynamics to calculate the Gibbs free energy G, the elastic constant matrix C_{ij} at a finite temperature can be derived from the Equation 2.33 by double deriving G with respect to strain components ε_{ij}. The value x, in this case is the temperature T, which is at room temperature [53].

$$C_{ij} = \frac{1}{V}\left(\frac{\partial^2 G}{\partial \varepsilon_i \varepsilon_j}\right)_x \tag{2.33}$$

Table 2.7.
Elastic stiffness constants (GPa) of this work and comparison with literature

Properties	**This work**	**Ref. [51] at 300K**	**Ref. [49]**	**Ref. [52] at 298K**	**Ref. [52] at 293K**
C11	269	295.9	294	297.08	298.5
C12	85	95.40	93	95.36	97.5
C13	85	n/a	n/a	n/a	n/a
C21	85	n/a	n/a	n/a	n/a
C22	269	n/a	n/a	n/a	n/a
C23	85	n/a	n/a	n/a	n/a
C31	85	n/a	n/a	n/a	n/a
C32	85	n/a	n/a	n/a	n/a
C33	269	n/a	n/a	n/a	n/a
C44	133	153.9	155	156.13	156.7
C55	133	n/a	n/a	n/a	n/a
C66	133	n/a	n/a	n/a	n/a

2.6.3 Vickers indentation result

The downward displacement of indenter into the substrate simulates the loading steps of indentation and upward displacement in positive y - direction represents unloading steps. The corresponding load value is achieved by summing the reaction forces of all the nodes along the base line of bulk materials or the substrate. The load versus displacement curves obtained from the FEM models is plotted in Fig.2.18 von-Mises stress distribution and elastic strain distribution are shown in figure 2.8 and figure 2.9 above. The stress was concentrated at the bottom of the indenter tip as a result of compressive pressure generated by the applied displacement and the deformation was relatively distributed over the indentation mark, because of the

compression relief during unloading. The stress - strain data through this period was plotted as shown in figure 2.19 and young's modulus (E ≈ 295 GPa) was calculated based on line-fitting technique while means diagonal diameter was found $d \approx 3.3m$ and $H_v \approx 16.58\,GPa$. The result agrees relatively with the value estimated through other simulations such as DFT and literature data of 245 GPa [54] and range of 270 to 330 GPa [55].

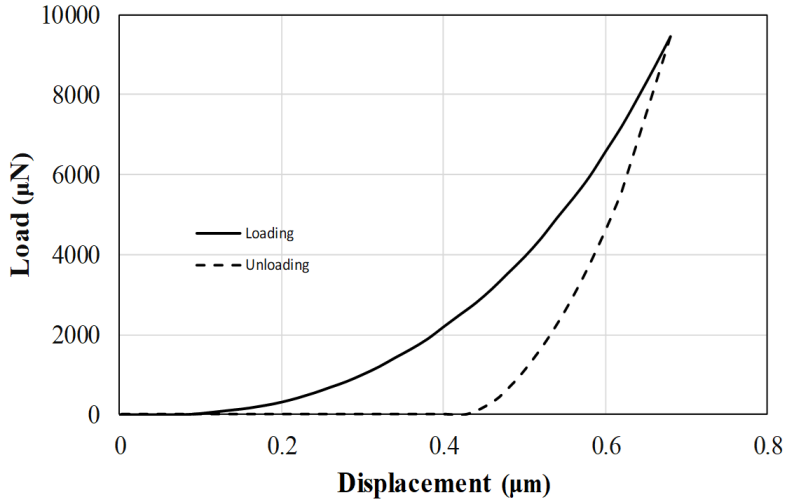

Fig. 2.18. Load vs. displacement curve for Vickers hardness model

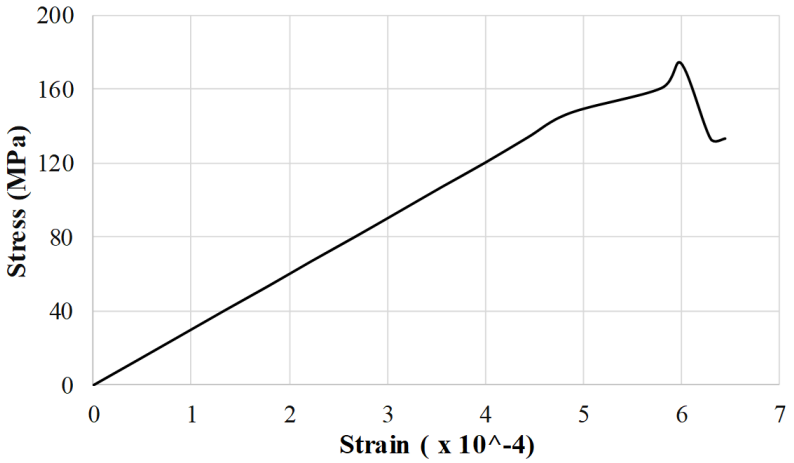

Fig. 2.19. Vickers simulation stress - strain curve

2.6.4 Brinell indentation result

von-Mises stress distribution and deformation distribution are shown in figure 2.12 and figure 2.13 above. Under loading, the stress was concentrated at the bottom of the indenter tip as a result of compressive pressure generated by the applied velocity and after unloading, the deformation was relatively distributed over the indentation mark, because of the compression relief during unloading process. The stress - strain data through the entire period was plotted as shown in figure 2.20 and young's modulus was calculated based on line - fitting technique. The result, as shown in table 2.8, agrees relatively with the value estimated through other simulations such as DFT and literature data of 227.58 GPa [48].

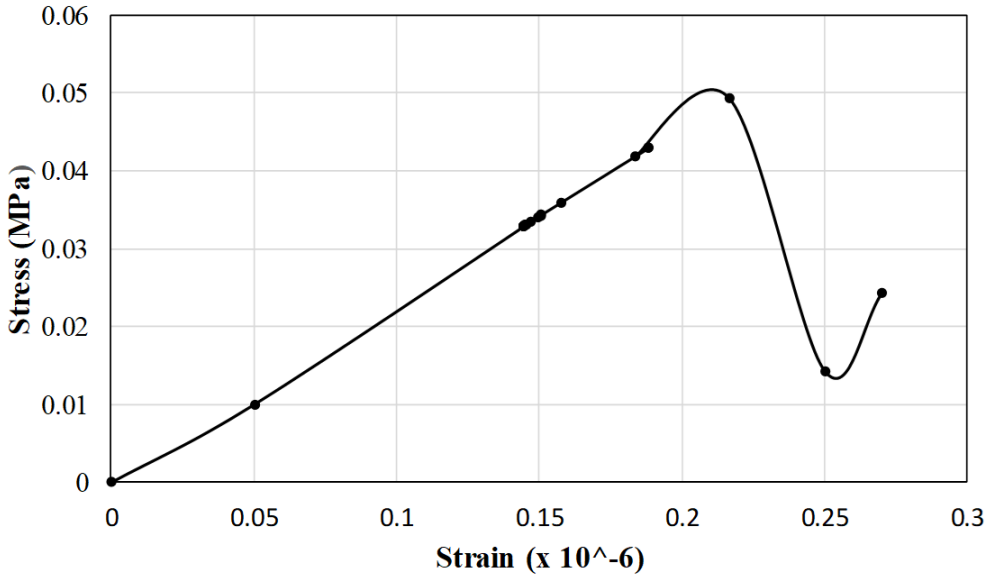

Fig. 2.20. Brinell's simulation stress - strain curve

Also, MgO hardness property was investigated based on force (1225 N) application on indenter and Brinell hardness number was determined approximately (16.1 HB

Table 2.8.
Experimental and literature data comparison

Data source	**Young's modulus**	**Poisson's ratio**	**Hardness value**
Ref [49]	249 (GPa)	0.18	N/A
This work (DFT)	228.803 (GPa)	0.2397	N/A
This work (FEM) Brinell's	226 (GPa)	N/A	(16.1 HB (5/125))
This work (FEM) Vicker's	295 (GPa)	N/A	16.58 GPa

Table 2.9.
Comparison between Brinell conversion table and our work using 5 mm indenter [56]

Indentation (mm)	**Load 750 (Kg)**	**Load 250 (Kg)**	**Load 125 (Kg)**	**Load 62.5 (Kg)**
2.96	98.4	32.8	16.4	8.2
2.97	97.7	32.6	16.3	8.1
2.98	96.9	32.3	16.2	8.1
2.99	96.2	32.1	16	8
3	95.5	31.8	15.9	8
3.01	94.8	31.6	15.8	7.9
This work $\approx$ 3.0	N/A	N/A	16.1	N/A

(5/125)) according to the equation (2.12) , compared with literature data of 16.0 HB (5/125) [56] as shown in table 2.9

2.6.5 Discrete element method results and discussion

The Compressive force (N), total energy (J), and angular velocity (rpm) of simulated particle to particle interaction is plotted in figure 2.21 within the same period on X- axis and other variables mentioned (Compressive force, total energy, and angular velocity) in Y - axis. It is clearly observed that each of these variables creates almost the same pattern up to 0.5s of simulated period, where relative variance begins as shown on the graph. However, at exactly 0.5s during DEM simulation, compressive force between the MgO particles reaches its maximum which creates maximum bond stress during particle to particle interactions. Also, angular velocity reaches its maximum which leads to maximum total energy as expected due to direct relationship between velocity and energy. The angular velocity can be found as 109013.1 rpm, and compressive force as 311 KN yields approximately 3000 MPa bond stress with predefined bounded radius of 5.8mm. The compressive strength of MgO - hydromagnesite (HY) system as 2200 - 2800 MPa [46, 47] is well below the simulated bond stress and therefore our model cannot withstand the stress the maximum bond stress during the simulation but failed .

Also, the coordination number and compressive force(N) during the DEM simulation of MgO reaches their maximum at approximately 0.5s as shown in figure 2.22 which agrees with the maximum number of immediate atoms surrounding a central atom at each position. This coordination number creates maximum compressive force as each atom contributes to the total compressive force at every time step during the simulation. Moreover, the average distance between each atom and the coordination number relatively remains constant through the rest of simulation period but the bond strength drops as it gradually breaks off from the surrounding atoms as compressive force reaches 274 KN and increases. Also, from the beginning of simulation to 0.45s, the compressive force is relatively zero as each atom experiences long distance from one another, but their coordination number gradually increases until 0.5s where the coordination number and distance between each atom attain relative steady state.

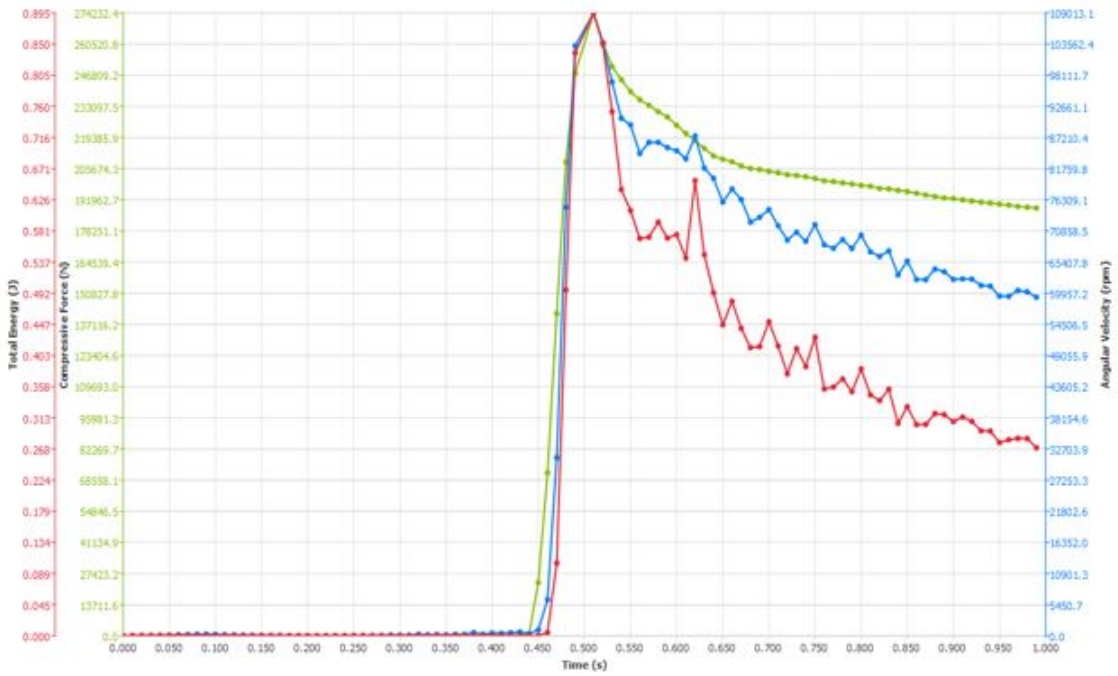

Fig. 2.21. Compressive force (N), total energy (J), and angular velocity (rpm) graph of simulated particle to particle interaction

The bond stress is determined from compressive force at each time step during the MgO simulation based on contact area between two atoms. The contact radius of 5.8 mm was defined, and it was used to calculate the bond stress as shown in table 2.11 which is plotted accordingly as shown in figure 2.23

Table 2.10.
MgO mechanical property simulation data

Simulation approach	**Young's modulus**	**Hardness value**	**Poisson's ratio**
MD	223 GPa	N/A	N/A
FEM (Vicker's)	295 GPa	16.58 GPa	N/A
FEM (Brinell's)	226 GPa	(16.1 HB (5/125))	N/A
DFT	228.8 GPa	N/A	0.2397

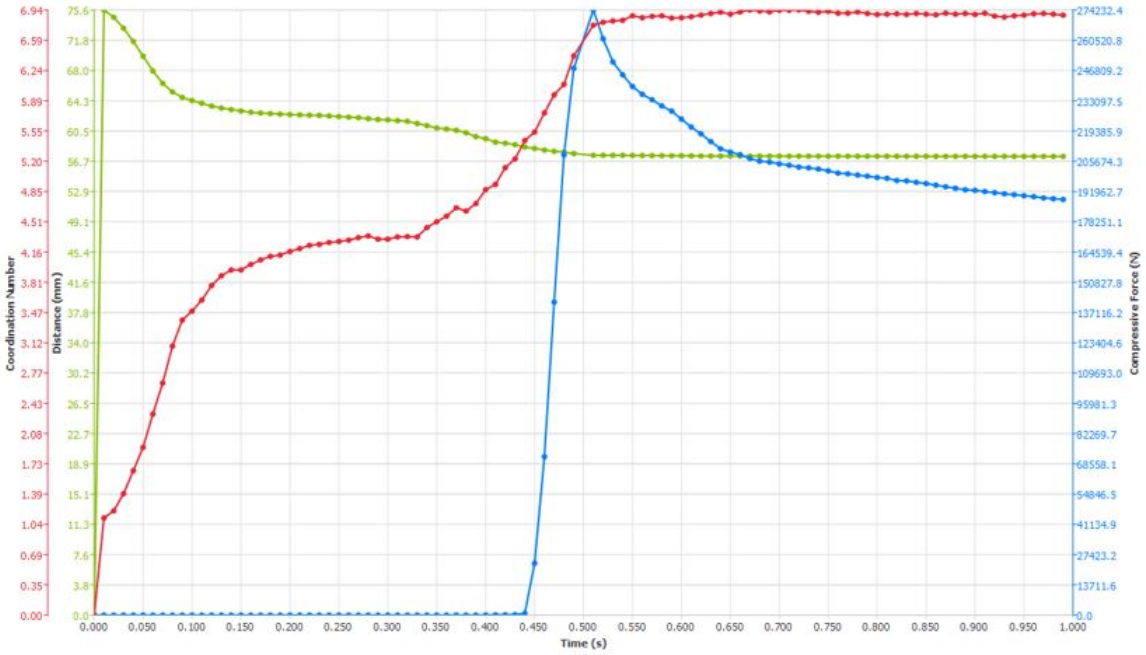

Fig. 2.22. Compressive force (N), coordination number, and distance (mm) graph of simulated particle to particle interaction

2.7 Conclusion

We have successfully established a robust simulation methodology to calculate the mechanical of MgO crystal using the molecular dynamic method, density functional theory through DFT code, finite element method using ANSYS, particle-based method through DEM. Most of the simulation results are summarized in table 2.10 and compared with experimental and modeling data in literature. The maximum bond stress of approximately 2960 MPa, and compressive force of 274 KN were obtained from this simulation, it can be induced that MgO bond strength is well below the maximum bond stress and after this stage, the bond gradually breaks off while the bond stress decreases accordingly. The sudden change in bond stress at 0.5s shows the reaction and quantity of bond strength present during the particle dislocation which steadily grows for the rest of simulation period. The stress - strain curve and

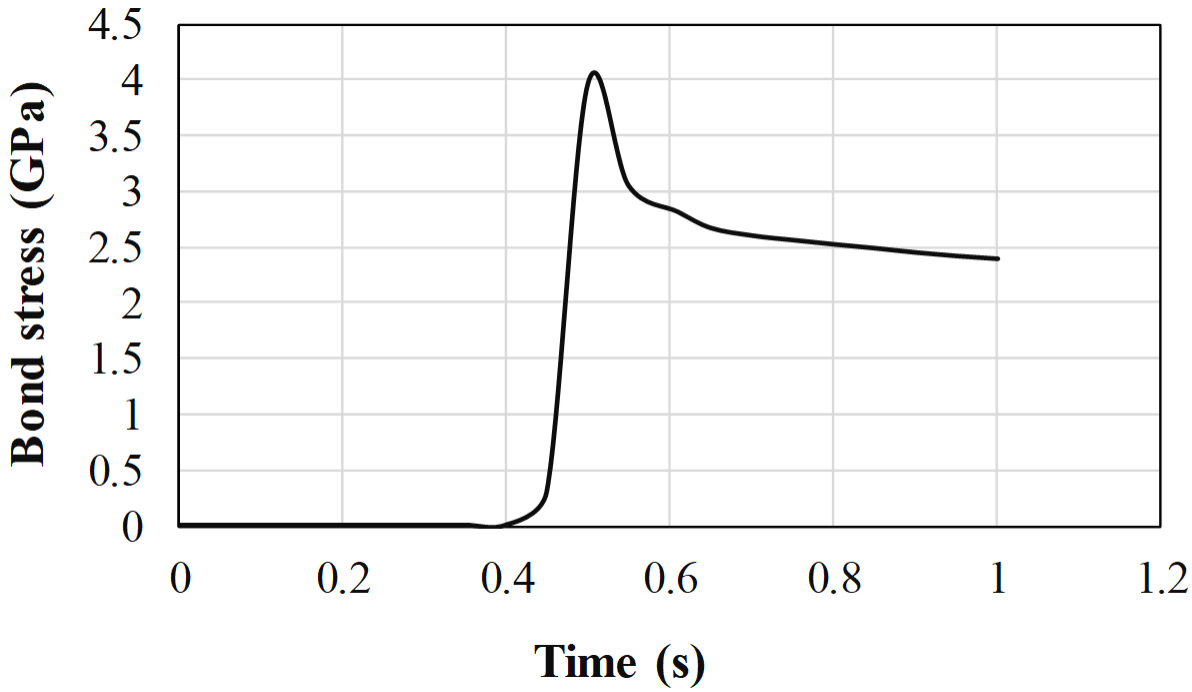

Fig. 2.23. Bond stress graph of simulated particle to particle interaction

young's modulus value, during atomistic simulation, shows that MgO may be a brittle material by experiencing permanent deformation during the 1st quarter of the tensile test and perhaps ceramic material. However, young's modulus values range from 223 GPa to 295 GPa from different simulation approach as shown in table 2.10.

Table 2.11.
DEM simulation data of MgO

Time (s)	**Compressive Force (N)**	**Bond Stress (Pa)**	**Total Energy (J)**
0	0	0	0
0.05	0.021818933	277.8072863	0.000665337
0.1	0.135390695	1723.84787	0.000452349
0.150001	0.142640018	1816.149113	0.000398718
0.2	0.13888774	1768.373626	0.000387764
0.250001	0.711794257	9062.845953	0.000385782
0.3	3.346436474	42608.15252	0.000383045
0.35	7.299826265	92944.2747	0.000361672
0.4	47.91512801	610074.3578	0.000435367
0.45	23503.33811	299253795.2	0.000392558
0.500001	311402.5767	3964900749	1.587564673
0.55	239572.3373	3050329736	0.610941914
0.61	221196.3416	2816359293	0.542507769
0.65	209842.3686	2671796019	0.446579079
0.7	204473.4686	2603437061	0.451142374
0.750001	201315.7726	2563232027	0.428732776
0.8	198302.4743	2524865520	0.383384299
0.850001	195567.053	2490037055	0.329142625
0.9	192491.7409	2450880965	0.307750887
0.95	190048.3059	2419770185	0.277530551
1	188043.0327	2394238254	0.274283399

3. THERMODYNAMIC AND PHYSICAL PROPERTIES OF MAGNESIUM OXIDE AND DOPED-MAGNESIUM OXIDE

3.1 DFT computational detail of MgO thermodynamic properties

Due to the development in density functional theory during the last two decades, it can now be used to calculate many properties of crystal structures. The Cambridge Serial Total Energy Package code is a sophisticated implementation of the density functional theory with pseudo potential using Generalized gradient approximation to obtain better results [57, 58]. GGA functionals are selected because they are more reliable than LDA functionals for predicting transition metal systems and it was used to calculate electronic properties of periodic systems, such as band structures and density of states (DOS). DFT Reflex code simulates X-ray, neutron, and electron powder diffraction patterns based on models of crystalline materials.

A computer program for the application of the method with X-ray data, or with neutron nuclear scattering data, has been written ab initio in an effort to make it versatile, and largely self-contained yet reasonably comprehensive result [59]. Thermodynamic properties were investigated from phonon calculation method through linear response with maximum number of phonon cycles (29 phonon vectors) were generated and energy for the crystal with each phonon vector was calculated. The Debye temperature can be extracted from the result and several temperature-dependent thermodynamic properties, including enthalpy, free energy, entropy, and specific heat capacity at constant volume, were calculated as shown in figure 3.1 and figure 3.2.

Thermodynamic properties are directly related with phonon structures and when calculating thermal properties of MgO, phonon calculation was performed with predefined displaced super cells and the forces on atoms of the set of supercells were

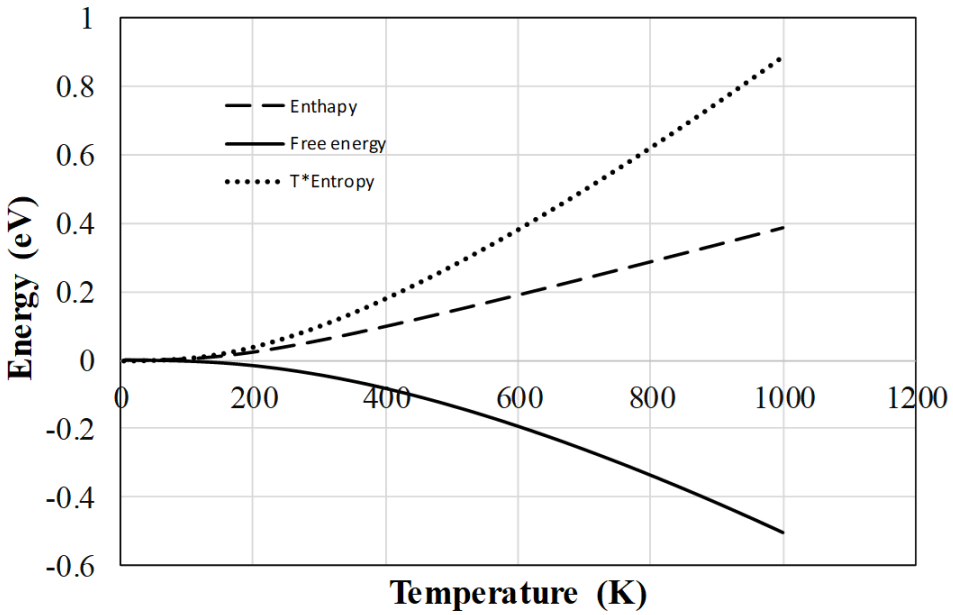

Fig. 3.1. Free energy, enthalpy and entropy of MgO

computed directly. Thus, entropy, enthalpy, free energy and heat capacity at constant volume were derived from phonon calculation which validates Gibbs free energy equation [60].

$$\Delta G^\circ = \Delta H^\circ - T\Delta S^\circ \tag{3.1}$$

$$G = U + PV - TS \tag{3.2}$$

where

$$F_z = U - TS$$

From the 1st law of thermodynamics

$$dU = dQ + dW = TdS - pdV \tag{3.3}$$

From

$$dU = d(ST) - SdT - pdV$$

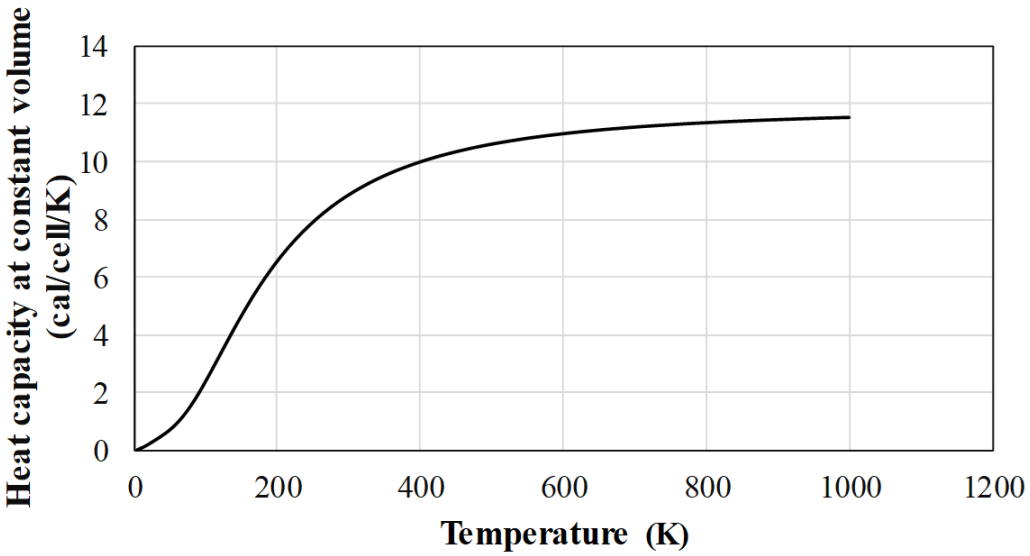

Fig. 3.2. Heat capacity at constant volume of MgO

Therefore,

$$dF_z = d(U - ST) = -SdT - pdV \tag{3.4}$$

$$F_z = \frac{1}{2}\Sigma_{(q,s)} h\omega(q,s) + k_B T \Sigma_{(q,s)} In[1 - \exp(-h\omega(q,s)/k_B T)] \tag{3.5}$$

$$S = -k_B T \Sigma_{(q,s)} In[1 - \exp(-h\omega(q,s)/(k_B T))] - \frac{1}{T}\Sigma_{(q,s)} \frac{h\omega(q,s)}{\exp\frac{h\omega(q,s)}{k_B T} - 1} \tag{3.6}$$

The change in Helmholtz free energy F, and entropy S are first calculated before Gibbs free energy. Also, the Debye temperature T_D is the temperature of a crystal's highest normal mode of vibration and at low temperatures, the heat capacity at constant volume is proportional to the cube of temperature satisfying the following equation [60].

$$C_v = 9Nk(\frac{T}{T_D})^3 \int_0^{T/T_D} \frac{x^4 e^x}{(e^x - 1)^2} dx \tag{3.7}$$

$$C_v = \Sigma(q,s) k_B [\frac{h\omega(q,s)}{k_B T}]^2 \frac{\exp[\frac{h\omega(q,s)}{k_B T}]}{[\exp\frac{h\omega(q,s)}{k_B T} - 1]^2} \tag{3.8}$$

where F is the Holmholtz free energy, S is entropy, C_v is heat capacity at constant volume, ω is natural frequencies of phonons, h is the Plank constant, k_B is the Boltzman constant and T is absolute temperature.

3.2 DFT computational detail of MgO physical properties

X-Ray Diffraction (XRD) is a method for characterization of microcrystalline samples to determine the crystallite size and identifying crystalline phases by processing the X-rays scattering from the crystalline solid, constructively interfere, and producing a diffracted pattern. This is based on the theory that crystalline substances act as 3-dimensional diffraction gratings for X-ray wavelengths similar to the spacing of planes in a crystal lattice as shown in figure 3.3 [61]. The X-ray diffraction simulation was performed on magnesium oxide and doped magnesium oxide structures, with doping effect of manganese, cobalt, nickel at 1.5%, 3%, 6%, and 12%. The diffraction patterns of relative intensity against angle of diffraction showing shift relationship between intensity and diffracted angle accordingly as explained by Bragg's law were investigated.

Bragg's law:

$$n\lambda = 2dsin$$

$$where\ n = 1, 2, 3, ...$$

$$\lambda = 2d \sin\theta \tag{3.9}$$

Hence,

$$d \propto \frac{1}{\theta}$$

Bragg angle is just the half of the total angle by which the incident beam is deflected. Bragg's law, as stated above, can be used to obtain the lattice spacing of a particular cubic system through the following relation

$$d = \frac{a}{\sqrt{h^2 + k^2 + l^2}} \tag{3.10}$$

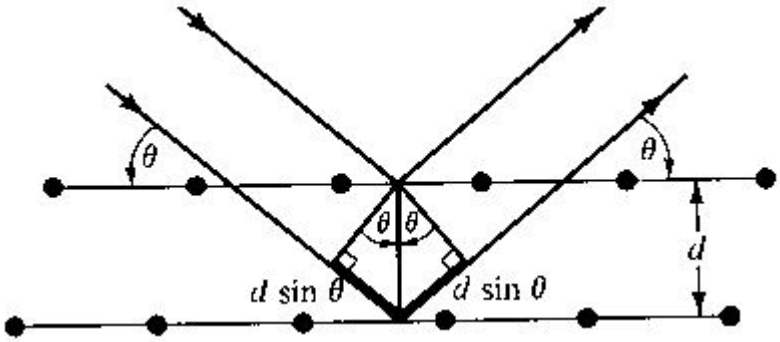

Fig. 3.3. Bragg's law illustration [62]

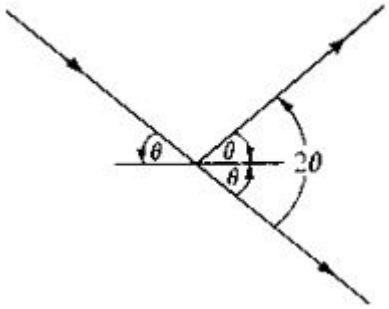

Fig. 3.4. Bragg's angle and 2θ illustration [62]

where λ is the wavelength of the radiation used, d is the inter-planar spacing involved and θ is the angle between the incident (or diffracted) ray and the relevant crystal planes; n is an integer, referred to as the order of diffraction, and is often unity, and h, k, and l are the Miller indices of the Bragg plane.

The electronic optimization of 2 x 2 x 2 supercell structure of MgO was first performed from the principle of strain-energy approach, with DFT code. Fast Fourier transformation, GGA and Perdew Burke Ernzerhof type of gradient exchange-correlation were selected in the calculations [63]. The Pseudo atomic calculation was then performed for Mg 2p6 3s2 and O 2s2 2p4. After geometry optimization, X-ray diffraction was calculated. Then, each composition of 1.5%, 3%, 6%, and 12% for each doping

element, manganese, cobalt, and nickel were compared with one another to establish phase shift relationship.

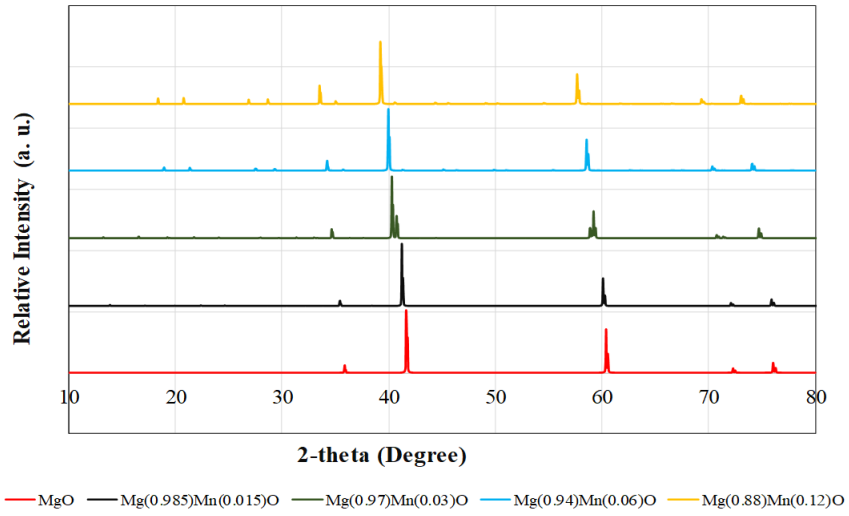

Fig. 3.5. XRD illustration of manganese doped - MgO

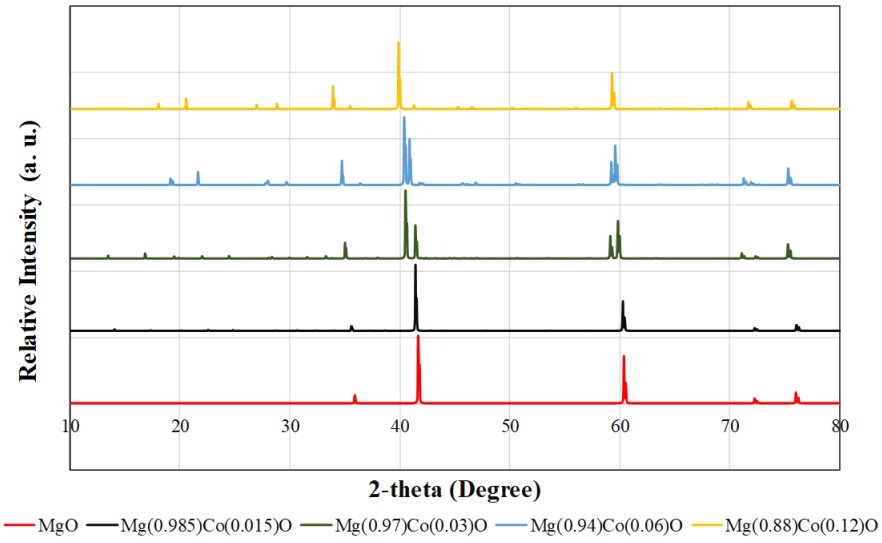

Fig. 3.6. XRD illustration of cobalt doped - MgO

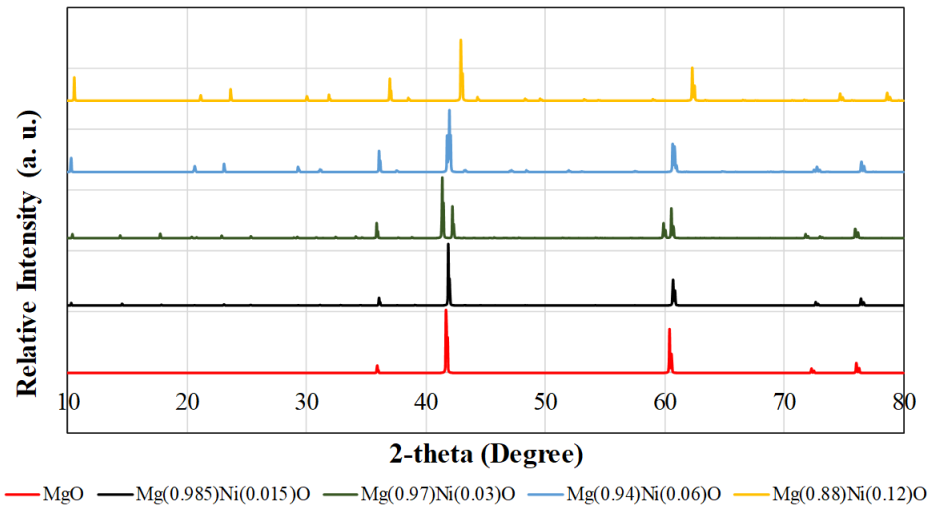

Fig. 3.7. XRD illustration of nickel doped- MgO

The X-ray diffraction simulation of manganese-doped magnesium oxide structures at 1.5%, 3%, 6%, and 12% were performed and the diffraction patterns of relative intensity against angle of diffraction showing peak backward shift between intensity and diffracted angle, as well as increased intensity in the doped structures accordingly as shown in figure 3.5. The cobalt-doped magnesium oxide structures at 1.5%, 3%, 6%, and 12% were also performed. The diffraction patterns of relative intensity against angle of diffraction showing peak backward shift between intensity and diffracted angle, as well as increased intensity in the doped structures accordingly but a lesser degree compared with manganese-doped structures as shown in figure 3.6. However, magnesium oxide and nickel-doped magnesium oxide structures at 1.5%, 3%, 6%, and 12% predicts diffraction patterns of relative intensity against angle of diffraction as peak forward shift between intensity and diffracted angle, as well as increased intensity in the doped structures accordingly.

3.3 Results and discussion of thermodynamic properties

Thermodynamic properties of MgO were carried out by DFT simulation package. At the beginning, in order to get accurate results, a geometry optimization was cautiously conducted. DFT module was used to calculate the lattice parameters based on energy minimization. Debye temperature, entropy, enthalpy, free energy and specific heat capacity under constant volume as temperature dependent variables were also determined.

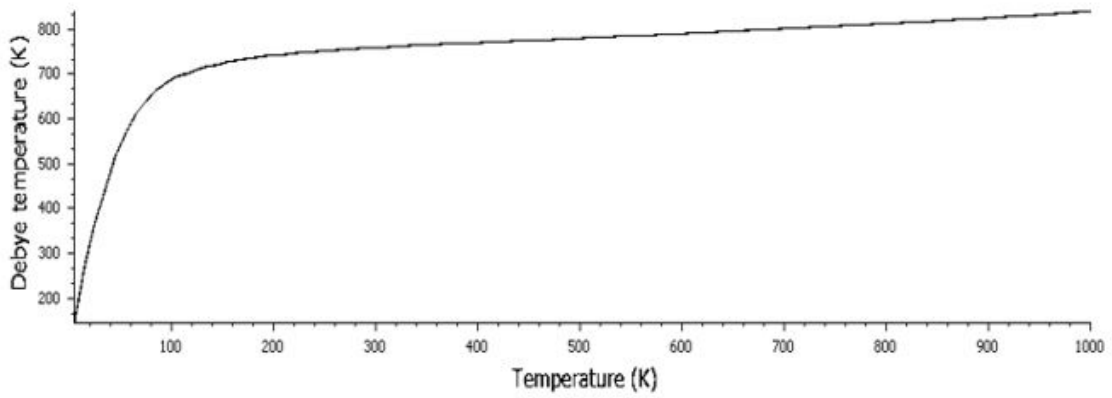

Fig. 3.8. Debye temperature of MgO from 0 to 1000K

Debye temperature of MgO from 0 to 1000 K was obtained as shown in figure 3.8 which predicts the highest mode of vibration of crystal during phonon vibration. With this data, specific heat at a constant volume can be calculated by differentiation with respect to temperature. With the Debye temperature, the thermodynamic properties of MgO were also obtained as shown in figure 3.1 - the enthalpy, entropy, free energy - and specific heat capacity at constant volume as dependent of temperature from 0 to 1000K are as well shown in figure 3.2. The specific heat at constant volume result from Debye temperature of 48.53 J/mol/K agree with literature data of 49.5 J/mol/K [64, 65].

3.4 Results and discussion of X - ray diffraction

X - ray diffraction patterns of MgO and doped - MgO structures were carried out by DFT simulation package. At the beginning, in order to get an accurate results, a geometry optimization was also conducted and DFT module was employed to calculate the lattice parameters based on energy minimization and reflex was then used to generate X - ray diffraction patterns accordingly. Relative intensity, in arbitrary unit, of different doped structures were plotted against reffracted angle 2θ and the results are shown in figure 3.5, figure 3.6 and figure 3.7. The relative intensity of manganese - doped structures against angle of diffraction showing peak backward shift while relative intensity of cobalt - doped structures against angle of diffraction also shows peak backward shift to a lesser degree between intensity and diffracted angle. However, while the relative intensity of nickel - doped structures against angle of diffraction predicts peak forward shift between intensity and diffracted angle, as well as increased intensity in the doped structures accordingly.

3.5 Conclusion

In this chapter, the first principles PBE-GGA calculations were performed to optimize the structure of MgO and doped - MgO crystal structures and investigate it's the crystallite size and identifying crystalline phases. The peak backward shift between intensity and diffracted angle of manganese - doped structures and cobalt - doped structures could be attributed to the ionic radius of doping manganese and cobalt which is greater than that of nickel accordingly, while the peak forward shift between intensity and diffracted angle of nickel - doped structures could also be attributed to the ionic radius. Also, the Gibbs energy, free enthalpy, and entropy up to 1000K shows good result and the specific heat capacity at constant volume of MgO as shown in figure 3.2 predicts about 11.6 Cal/cell/K (48.53 J/mol/K) in comparison with literature data of 49.5 J/mol/K. [64, 65].

4. MAGNETIC PROPERTIES OF MAGNESIUM OXIDE AND DOPED-MAGNESIUM OXIDE

In the present work, the magnetic properties of magnesium oxide crystal structure as refractory coating or non conductive material was studied. The relative comparison of substitutional doped-MgO in the form of Mg(1-x)M(x)O was as well investigated based on DFT approach. This is to improve the separation of the various turns or layers of the core material and prevent their sticking or welding together during high temperature anneals, aiding in the chemical purification of the ferrous material. Consequently, leading to develop the desired optimum magnetic characteristics of such material and forming a refractory-type coating which will provide insulation of one layer of ferrous material from the next. The transition metal doping elements M (Mn, Ni, or Co) in MgO were synthesized in various percentages and calculations were done through density functional theory. The magnetoelectric reactions of 2 by 2 by 2 doped supercells at x = 1.5 %, 3%, 6% and 12% were analyzed and compared. Figure 4.1 shows the relationship between these behaviors.

4.1 Computational method of magnetic properties of magnesium oxide

The basis cut-off energy was set to 340 eV. The structural, electronic, and magnetic properties of 2 x 2 x 2 supercells MgO, with k-points sampling grid in the first Brillouin Zone, were calculated based on density functional theory using the DFT code with the GGA in the scheme of Perdew-Burke-Eruzer (PBE) [66–68]. The electron-ion interactions were described by the Vanderbilt ultrasoft pseudopotential (USPP) and electronic configurations of 2p6 3s2 for magnesium and 2s2 2p4 for oxygen were used. The Pulay-type density mixing scheme was used for the electronic minimization and Monkhorst-Pack Scheme was used to sample the Brillouin zone.

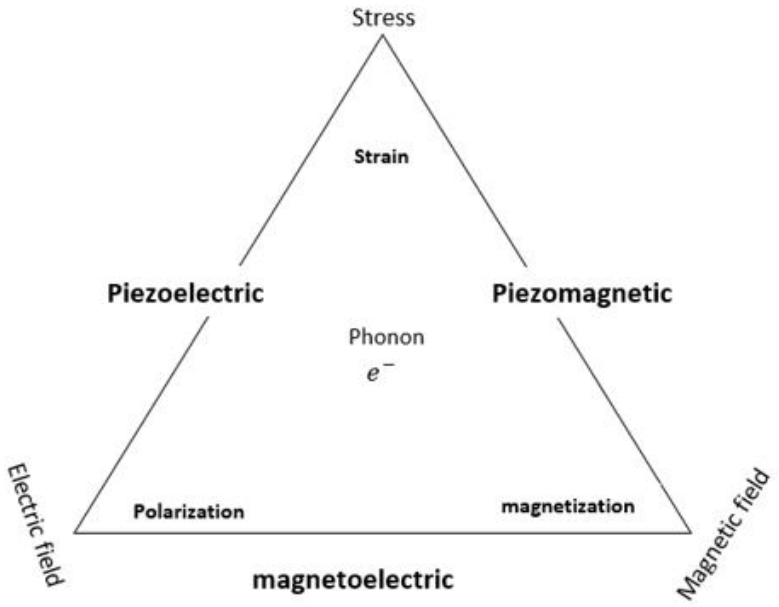

Fig. 4.1. Piezoelectric and piezomagnetic behavior

Geometry optimization was performed before the calculation of magnetic properties with consideration of spin polarization in all calculations. The convergence criterion for the optimization was based on maximum displacement, forces and stresses, with the forces per atom were reduced to 0.01 ev/A, and the maximum stress was below 0.02 GPa, and the displacement of atoms smaller than $0.05 \times 10^{-2}\dot{A}$, respectively.

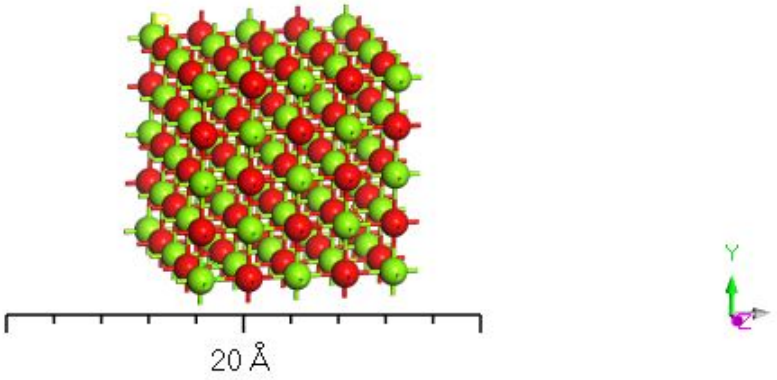

Fig. 4.2. 2 x 2 x 2 supercell structure of MgO. Green balls are magnesium while red balls are oxygen

A single electron rotating with an angular frequency ω_0 yields a current as follows [69]

$$i = \frac{e\omega_0}{2\pi} \tag{4.1}$$

Orbital magnetic moment

And from elementary magnetism, a current i passing in a loop of area A will produce an orbital magnetic moment μ_{orb} as follows [69]

$$\mu_{orb} = iA \tag{4.2}$$

Since electron moves in a circular pattern, therefore

$$\mu_{orb} = \frac{e\omega_0 r^2}{2} \tag{4.3}$$

But orbital angular moment $\Pi_0 = m_e\omega_0 r^2$;

Hence

$$\mu_{orb} = \frac{e\Pi_0}{2m_e} \tag{4.4}$$

Simplify the equation by multiply both numerator and denominator by $2\pi h$

$$\mu_{orb} = \frac{eh}{4\pi m_e}\frac{2\pi\Pi_0}{h} \tag{4.5}$$

$$\mu_{orb} = \mu_{orb}l \tag{4.6}$$

Where $eh/(4m_e)$ is known as Bohr magneton μ_B as the value of the orbital angular momentum of a single electron spinning around the Bohr atom.

Spin magnetic moment, μ_s

Electrons spin around themselves and produce spin magnetic moment as follows [69]

$$\mu_s = \frac{e\Pi_s}{m_s} \tag{4.7}$$

Both orbital angular moment Π_0 and spin angular moment Π_s must be an integer multiple of $\frac{h}{2\pi}$ and thus,

$$\mu_s = 2\mu_B s \tag{4.8}$$

where s is the spin quantum number; $s = \pm\frac{1}{2}$ and quantum mechanically

$$\mu_s = 2\mu_B\sqrt{s(s+1)} \tag{4.9}$$

Total magnetic moment, μ_{tot}

$$\mu_{tot} = \mu_s + \mu_{orb} \tag{4.10}$$

$$\mu_{tot} = \frac{e\Pi_s}{m_e} + \frac{e\Pi_0}{2m_e} \tag{4.11}$$

Tracthe total angular momentum J of the atom is the vector sum of the two noninteing momenta L and S_n, hence

$$J = L + S_n \tag{4.12}$$

However, the orbital angular momentum of the transition-metal ions of the 3d series that are responsible for most of the magnetic properties exhibited by ceramic materials is totally quenched and as a result [69].

$$J = S_n$$

$$\mu_{tot} = 2\mu_B\sqrt{S_n(S_n+1)} \tag{4.13}$$

where $S_n = \sum s$

4.2 Computational method of magnetic properties of doped systems

The substitutional doped 2 x 2 x 2 supercells of MgO with doping elements as Mn, Ni, or Co at various percentages of x = 1.5%, 3%, 6% and 12% in the form of Mg(1-x)M(x)O were investigated. The electron-ion interactions were also described by the Vanderbilt ultrasoft pseudopotential (USPP) and electronic configurations of

2p6 3s2 for magnesium, 2s2 2p4 for oxygen, 3d7 4s2 for cobalt, 3d8 4s2 for nickel and 3d5 4s2 for manganese were used respectively. The electronic and magnetic properties using DFT code with GGA in the scheme of Perdew-Burke-Eruzer (PBE), with k-points sampling grid in the first Brillouin Zone, were calculated based on density functional theory. Self-Consistent Formulism (SCF) was used in electronic minimization by treating the system as metallic with density mixing treatment of electrons. Pulay type of density-mixing scheme was employed and Ultra-soft pseudo potential was used in the calculations. The supercell originally consists 125 atoms in total (65 atoms of magnesium and 60 atoms of oxygen). Each dopant replaced each magnesium atom to create doping effects on the system. The manganese doped structures for various x-percentages are shown below accordingly.

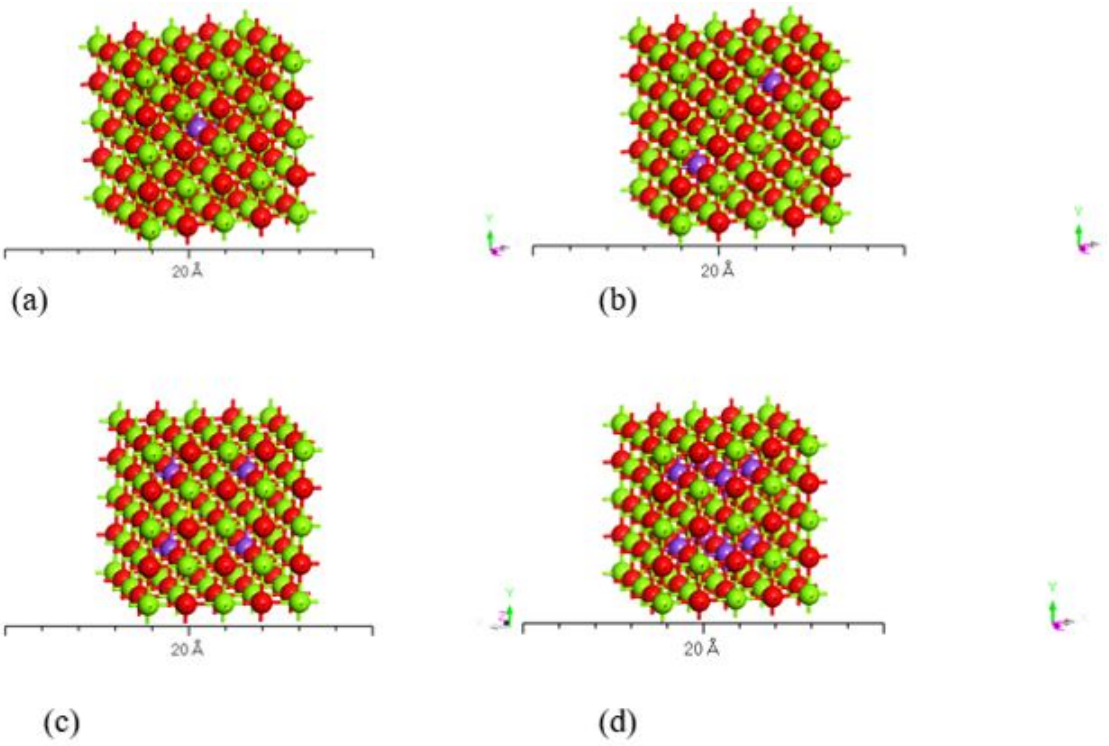

Fig. 4.3. Atomic structures of manganese-doped magnesium oxide. (a) 1.5%, (b) 3%, (c) 6%, (d) 12%. Green balls are magnesium, red balls are oxygen, purple are doping element, e.g., manganese

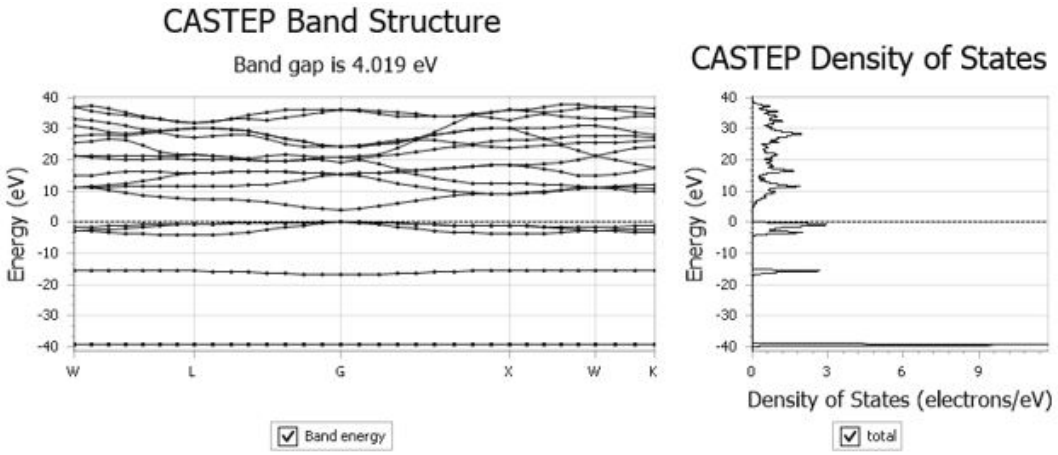

Fig. 4.4. Band structure and density of states of MgO

4.3 Models for the B-H relation of doped magnesium oxide via finite element method

The core of the single-phase E-core transformer was considered in this simulation, which form a closed magnetic flux path. The coils in the transformer was made of copper alloy, consists of 400 turns, placed around the central leg of the core as shown in figure 4.5. The model consists of backbar, keeper, poles which were made up of doped magnesium oxide properties in the form of Mg(1-x)M(x)O - where M is the doping element and coils through which input voltage was supplied in anti-clockwise direction. The enclosure box was made uniform by 50 mm which represents surrounding air and relatively medium mesh was selected and adaptive mesh option was chosen to improve accuracy. Then, the simulation was run in respect of the connection law in magnetic field and relative permeability of each doped magnesium oxide.

$$B = \mu_o(H + M_c) \tag{4.14}$$

where

$$M = \frac{\mu_{ion}}{V}$$

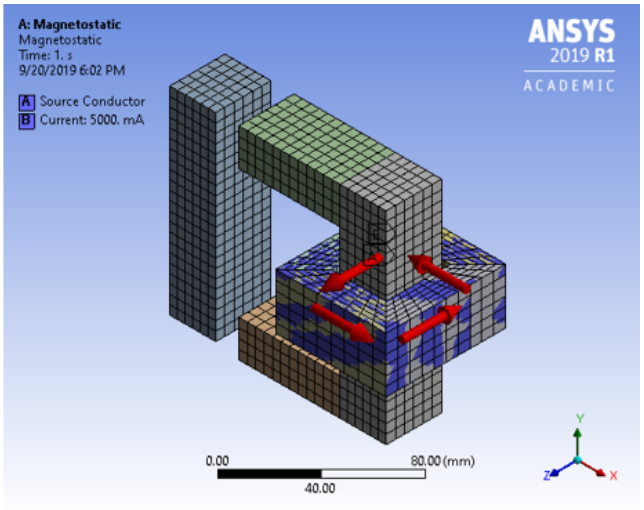

Fig. 4.5. B -H magnetization model

4.4 Results and discussion of magnesium oxide system

The mechanical and magnetic properties of 2 x 2 x 2 supercell structure of MgO were calculated first as the basis for further studies.

Table 4.1.
Mechanical and magnetic properties of MgO from DFT simulation

Property	**Value**
Final magnetic moment (B)	0.00
Band gap	4.019 eV
Bulk modulus	188.74 GPa
Energy cut off	340 eV
K point	0.04 $\dot{A}^{-1}$
Monkhorst Pack grids	8 x 8 x 8
k points in Berillouin Zone	60
Energy	-1413.658 eV

The properties were based on the first principles, calculated with the DFT simulation program. Basis sets and fast Fourier transformation and GGA and Perdew Burke Ernzerhof type of gradient Exchange-Correlation were selected in the calculations. The Pseudo atomic calculation was performed for Mg as 2p6 3s2 and O as 2s2 2p4 with geometry optimization. After geometry optimization, band structures, density of states, electronic and magnetic properties were calculated as shown in table 4.1. The conditions of interaction length distribution, the Hirshfeld analysis and atomic populations (Mulliken) are shown in table 4.3

Table 4.2.
Atomic populations (Mulliken) of MgO

Species	**Ion**	**s**	**p**	**d**	**f**	**Total**	**Charge (e)**
O	1	1.94	5.25	0.00	0.00	7.20	-1.20
Mg	1	0.59	6.22	0.00	0.00	6.80	1.20

Table 4.3.
Hirshfeld analysis and interaction length distribution of MgO

Species	**Ion**	**Hirshfeld Charge (e)**	**Spin (hbar/2)**
O	1	-0.34	0.00
Mg	1	0.34	0.00
Bond	**Population**	**Length (A)**	
O 1 – Mg 1	-2.38	2.16556	

4.5 Results and discussion of doped magnesium oxide systems

4.5.1 Doped system of Mg(1-x)Mn(x)O structure

The cutoff energy of 340 eV for computing charge density was based on fine criterion and 3 x 3 x 3 k-points sampling grid in the first Brillouin Zone of Mg(1-x)Mn(x)O structure was used in this calculation. The electronic, and magnetic properties of 2 x 2 x 2 supercell were calculated based on DFT code with GGA in the scheme of PBE. The electron-ion interactions were described by the Vanderbilt USPP with electronic configurations taken to be 2p6 3s2 for magnesium, 2s2 2p4 for oxygen, and 3d5 4s2 for manganese respectively [70]. The Monkhorst-Pack Scheme was used to sample the Brillouin zone and the Pulay-type density mixing scheme was used for the electronic minimization with consideration of spin polarization. Geometry optimization was initially performed before the calculation of doped Mg(1-x)Mn(x)O properties. Self-consistent field calculations were conducted with convergence criteria of the energy tolerance of 2 x 10^{-5}eV/atom. The geometry optimization was carried out until the forces acting on all atoms become lower than 0.03 eV/ $\dot{A}$ and the maximum displacement was 0.001 $\dot{A}$. The dopant percentage was chosen as 1.5%, 3%, 6% and 12% and each result is compared with one another as shown in table 4.4 .

The spin of each unpaired electrons from manganese ion Mn^{2+} yields about 4.4 hbar/2 atomic spin in comparison with the calculated magnetic moment of 5.92 [70]. The electronic configuration of Mn^{2+} has $3d^5$ in its orbital with 5 unpaired electrons having the spin quantum number (spin orientation). The final magnetic moment, band gap, and bulk modulus of each manganese-doped structures at 1.5%, 3%, 6%, and 12% are shown in table and its Hirshfeld analysis of Mg(0.94)Mn(0.06)O in table 4.5.

The calculated moment

$$\mu_{cal} = \sqrt{(n(n+2))}$$

where n is the unpaired electrons.

Table 4.4.
DFT simulation result of Mg(1-x)Mn(x)O

Property (Mg(1-x)Mn(x)O)	**x=1.5%**	**x=3%**	**x=6%**	**x=12%**
Final magnetic moment [B]	5.05912	6.05296	9.81991	20.0298
Band gap [eV]	1.089	0.029	0.791	1.131
Bulk modulus [GPa]	643.823	158.783	143.93017	138
Energy cut off [eV]	340	340	340	340
K point [A-1]	0.04	0.04	0.04	0.04
Monkhorst Pack grids	8 x 8 x 8	8 x 8 x 8	8 x 8 x 8	8 x 8 x 8
k points in Berillouin Zone	60	60	60	60
Energy [eV]	-44913.59	-22296.19	-10985.935	-21325.39

Table 4.5.
Hirshfeld analysis of Mg(0.94)Mn(0.06)O

Species	**Ion**	**Hirshfeld Charge (e)**	**Spin (hbar/2)**
O	1, 2	-0.33	-0.08
O	3, 4,5, 6	-0.34	-0.00
O	7, 8	-0.31	-0.15
Mg	1	0.35	-0.00
Mg	2,3,4, 5	0.34	-0.03
Mg	6	0.33	-0.01
Mg	7	0.34	-0.06
Mn	1, 2	0.28	-5.34

4.5.2 Doped system of Mg(1-x)Co(x)O structure

The doped structure of MgO by cobalt element for computing charge density was also based on cutoff energy of 340 eV with fine criterion, and 3 x 3 x 3 k-points sam-

pling grid in the first Brillouin Zone of Mg(1-x)Co(x)O structure. The electronic and magnetic properties of 2 x 2 x 2 supercell were calculated based on DFT code with the GGA in the scheme of PBE. The electron-ion interactions were described by the Vanderbilt USPP with electronic configurations taken to be 2p6 3s2 for magnesium, 2s2 2p4 for oxygen, and 3d7 4s2 for cobalt respectively [70]. The Monkhorst-Pack Scheme was used to sample the Brillouin zone and the Pulay-type density mixing scheme was used for the electronic minimization with consideration of spin polarization. Geometry optimization was initially performed before the calculation of doped Mg(1-x)Co(x)O properties. SCF calculations were conducted with convergence criteria of the energy tolerance of 2 x 10^{-5}eV/atom. The geometry optimization was carried out until the forces acting on all atoms become lower than 0.03 eV/ $\dot{A}$ and the maximum displacement was 0.001 $\dot{A}$. The dopant percentage was chosen as 1.5%, 3%, 6% and 12% and each result is compared with one another as shown in table 4.6.

Table 4.6.
DFT simulation result of Mg(1-x)Co(x)O

Property Mg(1-x)Co(x)O	**x=1.5%**	**x=3%**	**x=6%**	**x=12%**
Final magnetic moment [B]	2.0899	3.25039	6.982	12.6559
Band gap [eV]	0.372	0.096	0.861	1.231
Bulk modulus [GPa]	405.91	235.0796	222.04949	181.84
Energy cut off [eV]	340	340	340	340
K point [A-1]	0.04	0.04	0.04	0.04
Monkhorst Pack grids	8 x 8 x 8	8 x 8 x 8	8 x 8 x 8	8 x 8 x 8
k points in Berillouin Zone	60	60	60	60
Energy [eV]	-45301.376	-22683.814	-11373.88	-22877.112

The spin of each unpaired electrons from cobalt ion Co^{2+} yields about 3.25 hbar/2 atomic spin in comparison with the calculated magnetic moment of 3.87 [70]. The

electronic configuration of Co^{2+} has $3d^7$ in its orbital with 3 unpaired electrons having the same spin quantum number (spin orientation). The final magnetic moment, band gap, and bulk modulus of each cobalt-doped structures at 1.5%, 3%, 6%, and 12% are shown in table 4.6 and Hirshfeld analysis of Mg(0.88)Co(0.12)O is shown in table 4.7 .

Table 4.7.
Hirshfeld analysis of Mg(0.88)Co(0.12)O

Species	**Ion**	**Hirshfeld Charge (e)**	**Spin (hbar/2)**
O	1,2,3,4	-0.29	-0.14
O	5,6,7,8	-0.33	-0.00
O	9	-0.33	-0.01
O	10,11,12,13,14,15	-0.28	-0.08
Mg	1	0.33	-0.00
Mg	2,3,4,5	0.31	-0.02
Mg	6,7,8, 9	0.31	-0.01
Mg	10,11	0.32	-0.01
Mg	12	0.30	-0.02
Co	1,2,3,4	0.23	-3.25

4.5.3 Doped system of Mg(1-x)Ni(x)O structure

The doped structure of MgO by nickel element for computing the charge density was also based on cutoff energy of 340 eV with fine criterion, and 3 x 3 x 3 k-points sampling grid in the first Brillouin Zone of Mg(1-x)Ni(x)O structure. The electronic, and magnetic properties of 2 x 2 x 2 supercell were as well calculated based on DFT code with the GGA in the scheme of PBE. The electron-ion interactions were described by the Vanderbilt USPP with electronic configurations chosen to be 2p6

3s2 for magnesium, 2s2 2p4 for oxygen, and 3d8 4s2 for nickel respectively. The Monkhorst-Pack Scheme was used to sample the Brillouin zone and the Pulay-type density mixing scheme was also used for the electronic minimization with consideration of spin polarization. Geometry optimization was initially performed before the calculation of doped Mg(1-x)Ni(x)O properties. SCF calculations were conducted with convergence criteria of the energy tolerance of 2 x 10^{-5}eV/atom. The geometry optimization was carried out until the forces acting on all atoms become lower than 0.03 eV/ $\dot{A}$ and the maximum displacement was 0.001 $\dot{A}$. The dopant percentage was also chosen as 1.5%, 3%, 6% and 12% and each result is compared with one another as shown in table 4.8.

Table 4.8.
DFT simulation result of Mg(1-x)Ni(x)O

Property Mg(1-x)Co(x)O	**x=1.5%**	**x=3%**	**x=6%**	**x=12%**
Final magnetic moment [B]	2.20452	3.06388	4.78266	9.69509
Band gap [eV]	1.607	1.325	1.179	1.831
Bulk modulus [GPa]	313.964	159.8164	167.11802	155.213
Energy cut off [eV]	340	340	340	340
K point [A-1]	0.04	0.04	0.04	0.04
Monkhorst Pack grids	8 x 8 x 8	8 x 8 x 8	8 x 8 x 8	8 x 8 x 8
k points in Berillouin Zone	60	60	60	60
Energy [eV]	-45613.138	-22995.73	-11685.367	-24122.6395

The spin of each unpaired electrons from nickel ion Ni^{2+} yields about 2.27 hbar/2 atomic spin in comparison with the calculated magnetic moment of 2.83 [70]. The electronic configuration of Ni^{2+} has $3d^5$ in its orbital with 2 unpaired electrons having the same spin quantum number (spin orientation). The final magnetic moment, band gap, and bulk modulus of each nickel-doped structures at 1.5%, 3%, 6%, and 12% are shown table 4.8 Hirshfeld analysis of Mg(0.88)Ni(0.12)O shown in table 4.9.

Table 4.9.
Hirshfeld analysis of Mg(0.88)Ni(0.12)O

Species	**Ion**	**Hirshfeld Charge (e)**	**Spin (hbar/2)**
O	1,2,3, 4	-0.28	-0.14
O	5,6,7, 8	-0.34	-0.00
O	9	-0.33	-0.01
O	10, 11	-0.27	-0.09
O	12,13,14,15	-0.28	-0.06
O	16	-0.22	-0.16
Mg	1,2,3,4,5	0.32	-0.01
Mg	6,7,8,9,10,11	0.31	-0.01
Mg	12	0.30	-0.01
Ni	1,2,3,4	0.22	-2.27

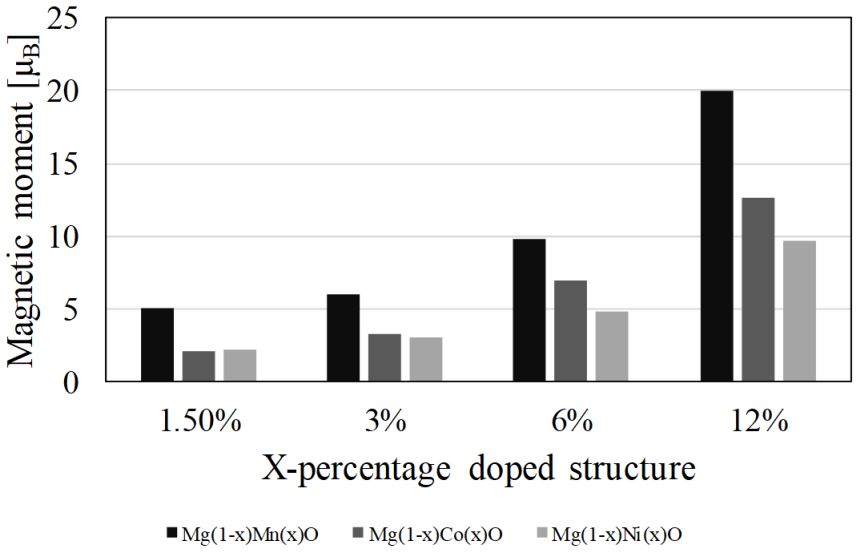

Fig. 4.6. Total magnetic properties of MgO - doped structures

Table 4.10.
Total magnetic moment [B] - doped MgO

Composition	**1.5%**	**3%**	**6%**	**12%**
Mg(1-x)Mn(x)O	5.05912	6.05296	9.81991	20.0298
Mg(1-x)Co(x)O	2.0899	3.25039	6.982	12.6559
(Mg(1-x)Ni(x)O	2.20452	3.06388	4.78266	9.69509

4.6 Results and discussion - B-H relation

The input voltage of 25 V in the copper alloy induced magnetic field intensity around the coils, which subsequently generates magnetic flux into the doped refractory material. The total magnetic flux density and corresponding field intensity is shown in figure 4.7 and table 4.11 as recorded after the simulation.

Table 4.11.
B -H comparison of doped magnesium oxide

Species	**Total magnetic field intensity (A/mm)**	**Total magnetic flux density (mT)**
Mg(0.88)Mn(0.12)O	178.43	1423.7
Mg(0.88)Co(0.12)O	175.37	1401.7
Mg(0.88)Ni(0.12)O	171.97	1377.2

4.7 Conclusion

We have successfully investigated mechanical, magnetic properties of doped magnesia crystal using DFT software. The properties were based on density functional theory using the DFT code with the GGA and results predicted from this method

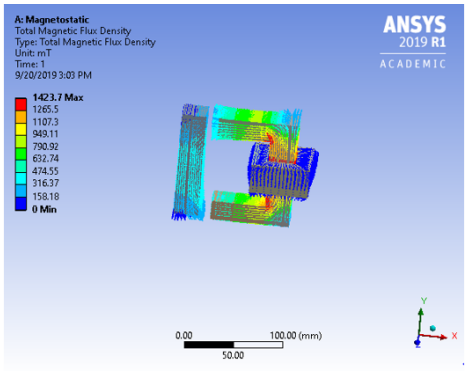

(a) (Mg(0.88)Mn(0.12)O) Magnetic flux density illustration

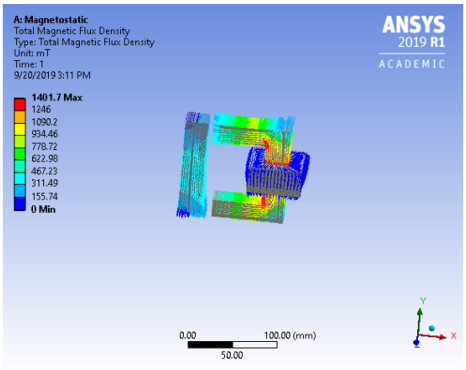

(b) (Mg(0.88)Co(0.12)O) Magnetic flux density illustration

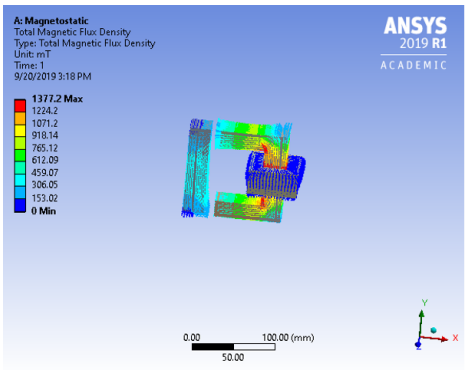

(c) (Mg(0.88)Ni(0.12)O) Magnetic flux density illustration.

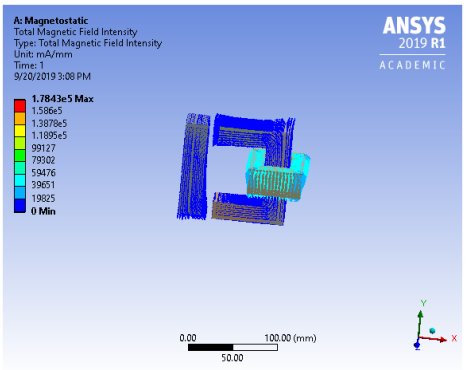

(d) (Mg(0.88)Mn(0.12)O) Magnetic field intensity illustration

Fig. 4.7. B -H comparison of doped magnesium oxide

agrees relatively with literature data as shown in table 4.4, table 4.6, and table 4.8 [70]. The magnetic property increases gradually as doping percentage increases with manganese doped structure found highest followed by cobalt doped structure, and nickel doped structure was found least both in DFT and continuum approach simulation using finite element method as shown in figure 4.6 and 4.7, while the bulk modulus of cobalt doped structure was found to be highest, followed by nickel doped and manganese doped structures respectively.

5. THERMAL PROPERTIES OF MAGNESIUM OXIDE

The study of temperature dependence of MgO properties is very important in understanding the temperature variation of other properties such as thermal conductivity, elastic constants, diffusion coefficients, and other heat transfer dimensionless numbers [71]. The thermal expansion of solids is of technical importance as it determines the thermal stability and thermal shock resistance of a material. According to Fourier's law, heat conduction $J_Q = -\kappa\nabla T$, determines the conducting heat flow density (J_Q) in the presence of a temperature gradient $\nabla T.\kappa$ [72]. In this chapter, we investigated the first-principles study of lattice thermal conductivity of MgO using the first principles imposed-flux method in DFT Forcite code.

5.1 DFT computational detail of thermal properties

The initial structure was first optimized with forcefield assignment as charges to minimize the energy and ensure more accurate results. Then, the thermal conductivity was calculated based on the Reverse Non-Equilibrium Molecular Dynamics (RNEMD) method. This method works on the basis of velocity exchanges between two molecules in different parts of the simulation cell and thus, the velocity of the fastest atom (or molecule) in one region is replaced by the velocity of the slowest atom in another region, at a set interval, and vice versa. Consequently, the first region becomes colder, whereas the second region increases in temperature. The system reacts by flowing energy from the hot to the cold region. Eventually a steady state was established when the energy exchanged offsets the energy flowing back with a temperature gradient over the space between the two regions. The thermal conductivity follows as the energy flux divided by the temperature gradient. Consequently, energy flows between the layers and system responds by creating a temperature gra-

dient. There are 40 layers of atoms in z-direction using variable exchange method to transfer energy. The simulation follows the Fourier's law [73] as stated in equation 5.1 and the parameters used were stated in table 5.1.

Table 5.1.
Parameters for MgO thermal conductivity calculation

Parameter	**Value**
Type of exchange method	Variable
Type of velocity to exchange	Atoms
Energy to exchange in the method FIXED	1.0 (in kcal/mol)
Number of exchanges performed for equilibration	500
Number of exchanges performed for production	1000
Number of exchanges between two field updates	10
Number of time steps between two exchanges	100
Timestep	1 (in fs)

$$\frac{\Delta Q}{\Delta t} = -K_{th} A \frac{\Delta T}{\Delta x} \tag{5.1}$$

where $\frac{\Delta Q}{\Delta t}$ (GW) is the heat transferred rate; A (m^2) is the cross section area; K_{th} (W(mK))is the thermal conductivity; x (m) is distance between two ends; and $\frac{\Delta T}{\Delta x}$ (K/m) temperature gradient along x axis.

5.2 Results and discussion of thermal properties

The thermal conductivity of MgO was calculated using the imposed-flux method [74]. Kinetic energy is exchanged between one or more particles in a hot layer (red) and a cold layer (blue), imposing an energy flux through the system as shown in figure 5.1 and temperature distribution in z - direction as shown in figure 5.2. The layers are repeated due to periodic boundary conditions

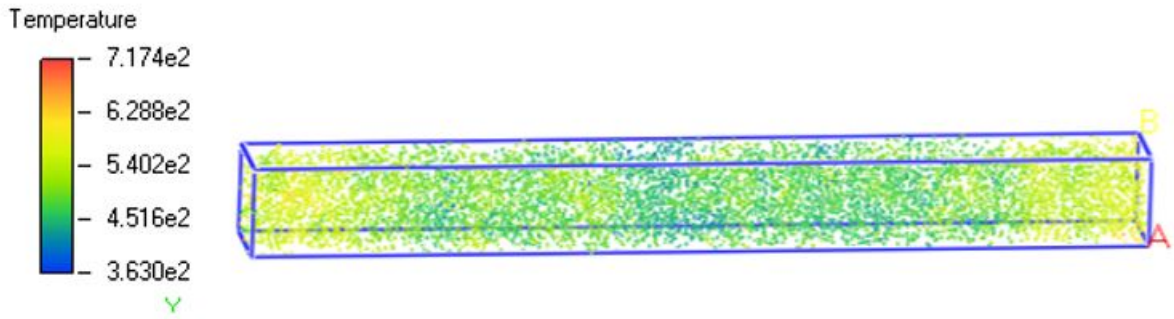

Fig. 5.1. Temperature distribution (unit: K)

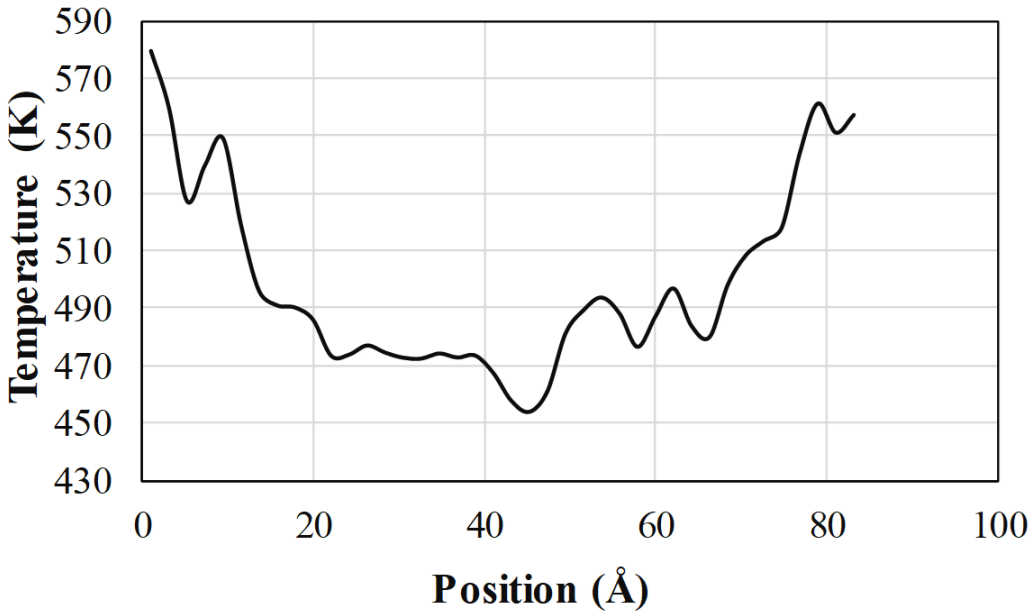

Fig. 5.2. Temperature distribution along z-axis

The energy flux curve became flat after 200 ps, which means the entire system is stable. Thus, temperature distribution along the z - direction of MgO super cell is plotted in Fig 5.2 and the curve shows the heat flux is in relative linear relationship with position from high temperature to low temperature, and support temperature

gradient in the Fourier's law. The calculated temperature gradient was 5.1 GK/m, the energy flux was 177 GW/m^2. So thermal conductivity was the ratio of energy flux to temperature gradient, which was 34.63 W/m/K.

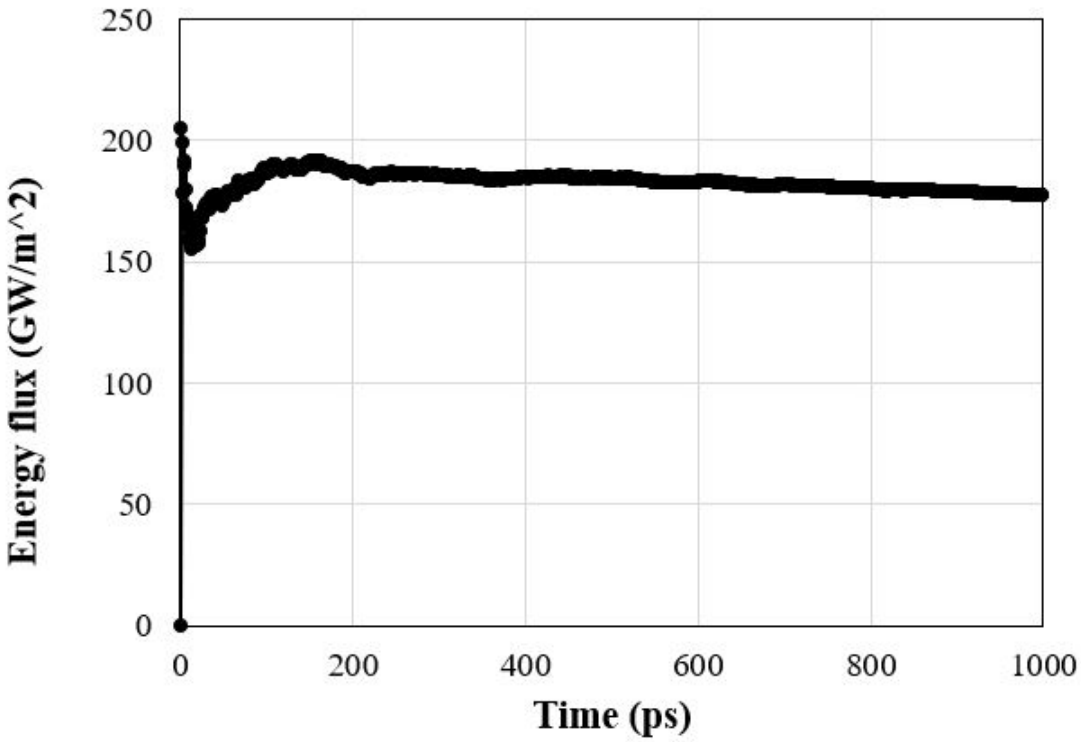

Fig. 5.3. Energy flux time history

5.3 Conclusion

The Reverse Non-Equilibrium Molecular Dynamics (RNEMD) method was successfully established as a robust simulation methodology to calculate thermal properties of MgO crystal using DFT software through Forcite code. The methodology allows us to simulate temperature gradient and the energy flux of MgO crystal structure within a specific temperature range and the thermal conductivity was calculated to be 34.63 W/m/K which in agreement with literature data [75].

6. SUMMARY

In this thesis, a modeling study is conducted to understand the mechanical, thermodynamic, magnetic and thermal properties of pure and M-doped (M stands for Mn, Co, or Ni) magnesia. The work can be used to design improved coatings for electrical transformers in the future. The major conclusions are summarized below.

1. For the mechanical properties of pure magnesia, using density functional theory (DFT) based calculations, the computed Youngs modulus, Poissons ratio, bulk modulus, and compressibility are 228.80 GPa, 0.2397, 146.52 GPa, and 0.00682, respectively, which are in good agreement with the literature data. Using molecular dynamics (MD) simulations, the computed Youngs modulus is 229 GPa. Using discrete element model (DEM) approach, the bending deformation of magnesia is simulated. Finally, using finite element model (FEM), micro-hardness indentation of magnesia is simulated, and the computed Brinell hardness is 16.1 HB, and Vickers hardness is 16 GPa.

2. For the thermodynamic and physical properties of pure and doped magnesia, using DFT based simulations, the temperature-dependent thermodynamic properties, such as free energy, enthalpy, entropy, heat capacity at constant volume, and Debye temperature of magnesia, are computed. The X-ray powder diffraction (XRD) spectra of M-doped magnesia are simulated, at the doping level of 1.5%, 3%, 6% and 12%, respectively. The simulated XRD data show that peaks shift to higher angles as the doping level increases.

3. For the magnetic properties of pure and doped magnesia, using DFT based simulations, the calculated magnetic moments increase with the doping level, with Mn as the highest, followed by Co and Ni. This is due to the fact that Mn has more unpaired electrons than Co and Ni.

4. For the thermal properties of the pure magnesia, using the Reverse Non-Equilibrium Molecular Dynamics (RNEMD) method, the computed thermal conductivity of magnesia is 34.63 W/m/K, which is in agreement with the literature data of 33.0 W/m/K at 400 K.

7. RECOMMENDATIONS

We have successfully investigated mechanical and magnetic properties of doped magnesia crystal using DFT and continuum approach. The properties were based on density functional theory with the GGA and results predicted from this method agrees with literature data as shown in table 4.10 [70]. The magnetic property increases gradually as doping percentage increases with manganese doped structure found highest followed by cobalt doped structure, and nickel doped structure was found least both in DFT and continuum approach simulation while the bulk modulus of cobalt doped structure was found to be highest, followed by nickel doped and manganese doped structures respectively. Manganese doped structure was concluded to generate more magnetic flux as refractory coatings on transformer core. However, other factors such as electrical insulation according to band gap, and mechanical properties could make cobalt doped structure and nickel doped structure more reliable to manganese doped structure depending on the prime factor.

It is therefore recommended to perform future research on electrical insulation of transformer core from continuum approach in supporting the DFT conclusion according to the present work.

REFERENCES

REFERENCES

[1] C. Krause, "Power transformer insulation–history, technology and design," *IEEE Transactions on Dielectrics and Electrical Insulation*, vol. 19, no. 6, pp. 1941–1947, 2012.

[2] H. Yi-Yan, J. Hong-Wei, Z. Dong-Bai, and Y. Jia-Xiang, "The rapid development of the transformer industry in china," *IEEE Electrical Insulation Magazine*, vol. 14, no. 4, pp. 23–27, 1998.

[3] M. Guarnieri, "Who invented the transformer?[historical]," *IEEE industrial electronics magazine*, vol. 7, no. 4, pp. 56–59, 2013.

[4] J. Acero, J. Alonso, R. Araujo, F. Auat Cheein, F. Azcondo, F. Baronti, I. Bertolotti, G. Biswal, F. Blaabjerg, D. Boroyevich *et al.*, "2013 index ieee industrial electronics magazine vol. 7," *Power Electronics*, p. 61, 2013.

[5] L. Balansay, "Transformer core," *EE IIT*, 2014.

[6] Kharagpur, *Magnetic Circuits and Core Losses*. EE IIT: Addison-Wesley, 1994.

[7] P. Parthasaradhy and S. Ranganayakulu, "Hysteresis and eddy current losses of magnetic material by epstein frame method-novel approach," *The International Journal of Engineering and Science*, pp. 85–93, 2014.

[8] H. M. Elsey and C. C. Horstman, "Process of coating ferrous silicon magnetic material," Feb. 5 1946, uS Patent 2,394,047.

[9] S. W. Sopp, L. S. Lee, and M. W. Howe, "Magnesium oxide composition for coating silicon steel," Apr. 17 1984, uS Patent 4,443,425.

[10] R. Morjan and S. Prasalovich, "Em4: Magnetic hysteresis," *Lab version*, vol. 1, 2003.

[11] Y. Li, Q. Yang, and J. Zhu, "Three-dimensional magnetic properties measurement of the laminated silicon steels," in *2015 IEEE International Magnetics Conference (INTERMAG)*. IEEE, 2015, pp. 1–1.

[12] V. Pocajt, "Silicon steels and their applications," *Total material*, 2003.

[13] K. Lin and J.-S. Hsu, "Selection of silicon steel for transformer cores," in *Proceedings: Electrical Electronics Insulation Conference and Electrical Manufacturing & Coil Winding Conference*. IEEE, 1995, pp. 147–152.

[14] M. Amini and M. P. Moghaddam, "Probabilistic modelling of electric vehicles' parking lots charging demand," in *2013 21st Iranian Conference on Electrical Engineering (ICEE)*. IEEE, 2013, pp. 1–4.

[15] Y. Oda, M. Kohno, and A. Honda, "Recent development of non-oriented electrical steel sheet for automobile electrical devices," *Journal of Magnetism and Magnetic Materials*, vol. 320, no. 20, pp. 2430–2435, 2008.

[16] S. Magdaleno-Adame, T. D. Kefalas, S. Garcia-Martinez, and C. Perez-Rojas, "Electromagnetic finite element analysis of electrical steels combinations in lamination core steps of single-phase distribution transformers," in *2017 IEEE International Autumn Meeting on Power, Electronics and Computing (ROPEC)*. IEEE, 2017, pp. 1–5.

[17] W. H. Bartley, "Analysis of transformer failures, proceedings of the thirty six annual conference," *Proceedings of the Thirty Six Annual Conference*, 2003.

[18] C. Ndungu, J. Nderu, L. Ngoo, and P. Hinga, "A study of the root causes of high failure rate of distribution transformer-a case study," *International Journal Engineering and Science*, vol. 2, pp. 14–18, 2017.

[19] J. F. Steger, "Magnesium oxide coating composition and process," Jan. 13 1976, uS Patent 3,932,201.

[20] C. Carrander, "Magnetizing currents in power transformers: Measurements, simulations, and diagnostic methods," Ph.D. dissertation, KTH Royal Institute of Technology, 2017.

[21] L. S. Lee, Y. Uyeda, and L. F. Heneghan, "Magnesium oxide coatings," Oct. 10 1972, uS Patent 3,697,322.

[22] N. Leuning, S. Steentjes, K. Hameyer, B. Gerhards, and U. Reisgen, "Analysis of a novel laser welding strategy for electrical steel laminations," in *2017 7th International Electric Drives Production Conference (EDPC)*. IEEE, 2017, pp. 1–8.

[23] A. Moses, "Electrical steels: past, present and future developments," *IEE Proceedings A (Physical Science, Measurement and Instrumentation, Management and Education)*, vol. 137, no. 5, pp. 233–245, 1990.

[24] N. P. Goss, "Electrical sheet and method and apparatus for its manufacture and test," Jul. 3 1934, uS Patent 1,965,559.

[25] A. Moses, S. Pegler, and J. Thompson, "Role of phosphate coating in determining the magnetic properties of goss-oriented silicon iron," in *Proceedings of the Institution of Electrical Engineers*, vol. 119, no. 8. IET, 1972, pp. 1222–1228.

[26] Y.-G. Jung, "Private communication on experimental procedures for synthesized mgo," Changwon national university, july 2019.

[27] C. Ostrouchov, "dftfit documentation, release 0.3.2." *Release 0.3.2*, 2018.

[28] M. P. Allen *et al.*, "Introduction to molecular dynamics simulation," *Computational soft matter: from synthetic polymers to proteins*, vol. 23, pp. 1–28, 2004.

[29] C. Ostrouchov, "potentials documentation, release 0.1," *Release 0.1*, 2018.

[30] D. Fincham, "Leapfrog rotational algorithms," *Molecular Simulation*, vol. 8, no. 3-5, pp. 165–178, 1992.

[31] R. R. Reeber, K. Goessel, and K. Wang, "Thermal expansion and molar volume of mgo, periclase," *Eur. J. Mineral*, vol. 7, pp. 1039–1047, 1995.

[32] A. Pedone, G. Malavasi, M. C. Menziani, A. N. Cormack, and U. Segre, "A new self-consistent empirical interatomic potential model for oxides, silicates, and silica-based glasses," *The Journal of Physical Chemistry B*, vol. 110, no. 24, pp. 11 780–11 795, 2006.

[33] H. Gou, L. Hou, J. Zhang, and F. Gao, "Pressure-induced incompressibility of rec and effect of metallic bonding on its hardness," *Applied Physics Letters*, vol. 92, no. 24, p. 241901, 2008.

[34] D. M. Teter, "Computational alchemy: the search for new superhard materials," *Mrs Bulletin*, vol. 23, no. 1, pp. 22–27, 1998.

[35] J. Tse, "Intrinsic hardness of crystalline solids," *Journal of Superhard Materials*, vol. 32, no. 3, pp. 177–191, 2010.

[36] S. R. Low, K. Hattori, A. Germak, and A. Knott, "Proposed definition for the brinell hardness indentation edge," *ACTA IMEKO*, vol. 3, no. 3, pp. 3–8, 2014.

[37] M. Liu, J.-y. Lin, C. Lu, K. Tieu, K. Zhou, and T. Koseki, "Progress in indentation study of materials via both experimental and numerical methods," *Crystals*, vol. 7, no. 10, p. 258, 2017.

[38] M. M. Dhaigude, "Anvil effect in spherical indentation testing on sheet metal," Ph.D. dissertation, Texas A&M University, 2006.

[39] D. O. Potyondy and P. Cundall, "A bonded-particle model for rock," *International journal of rock mechanics and mining sciences*, vol. 41, no. 8, pp. 1329–1364, 2004.

[40] D. O. Potyondy, "Simulating stress corrosion with a bonded-particle model for rock," *International Journal of Rock Mechanics and Mining Sciences*, vol. 44, no. 5, pp. 677–691, 2007.

[41] J. Yoon, "Application of experimental design and optimization to pfc model calibration in uniaxial compression simulation," *International Journal of Rock Mechanics and Mining Sciences*, vol. 44, no. 6, pp. 871–889, 2007.

[42] J.-W. Park and J.-J. Song, "Numerical simulation of a direct shear test on a rock joint using a bonded-particle model," *International Journal of Rock Mechanics and Mining Sciences*, vol. 46, no. 8, pp. 1315–1328, 2009.

[43] M. P. Schöpfer, S. Abe, C. Childs, and J. J. Walsh, "The impact of porosity and crack density on the elasticity, strength and friction of cohesive granular materials: Insights from dem modelling," *International Journal of Rock Mechanics and Mining Sciences*, vol. 46, no. 2, pp. 250–261, 2009.

[44] P. A. Cundall, "A discontinuous future for numerical modelling in geomechanics?" *Proceedings of the institution of civil engineers-geotechnical engineering*, vol. 149, no. 1, pp. 41–47, 2001.

[45] Y. Ouyang, Q. Yang, and X. Chen, "Bonded-particle model with nonlinear elastic tensile stiffness for rock-like materials," *Applied Sciences*, vol. 7, no. 7, p. 686, 2017.

[46] J. Watson, F. Wiffen, J. L. Bishop, and B. K. Breeden, "Radiation effects and tritium technology for fusion reactors. volume i. proceedings of the international conference, gatlinburg, tennessee, october 1–3, 1975," Oak Ridge National Lab., Tenn.(USA), Tech. Rep., 1976.

[47] F. H. D. Zhang, *Magnesium oxide based binders as low-carbon cements*. Imperial College London, 2013.

[48] R. Gaillac and F.-X. Coudert, *ELATE: Elastic tensor analysis*. 10.1088/0953-8984/28/27/275201: IOP Publishing, May 2016.

[49] Crystran, *Magnesium Oxide (MgO) - Crystran*. Business Park, Poole, Dorset: Crystran Manufacture, 2012.

[50] L. Wu and J. Zhang, "Ab initio study of anisotropic mechanical properties of licoo2 during lithium intercalation and deintercalation process," *Journal of Applied Physics*, vol. 118, no. 22, p. 225101, 2015.

[51] K. Marklund and S. A. Mahmoud, "Elastic constants of magnesium oxide," *Physica Scripta*, vol. 3, no. 2, pp. 75–76, feb 1971. [Online]. Available: https://doi.org/10.1088%2F0031-8949%2F3%2F2%2F005

[52] Y. Sumino, O. L. Anderson, and I. Suzuki, *Temperature coefficients of elastic constants of single crystal MgO between 80 and 1,300 K*. Physics and Chemistry of Minerals, Jan 1983.

[53] J. F. Nye *et al.*, *Physical properties of crystals: their representation by tensors and matrices*. Oxford university press, 1985.

[54] D. Zhu, N. S. Jacobson, and R. A. Miller, "Thermal-mechanical stability of single crystal oxide refractive concentrators for high-temperature solar thermal propulsion," 1999.

[55] Goodfellow, "Magnesia - magnesium oxide (mgo) properties and applications," 10 2019.

[56] M. Middleton, *Brinell Hardness Tester Model, NB-3010*. Newage hardness testing, 2016.

[57] M. Segall, P. J. Lindan, M. a. Probert, C. J. Pickard, P. J. Hasnip, S. Clark, and M. Payne, "First-principles simulation: ideas, illustrations and the castep code," *Journal of Physics: Condensed Matter*, vol. 14, no. 11, p. 2717, 2002.

[58] J. P. Perdew and Y. Wang, "Accurate and simple analytic representation of the electron-gas correlation energy," *Physical Review B*, vol. 45, no. 23, p. 13244, 1992.

[59] D. t. Wiles and R. Young, "A new computer program for rietveld analysis of x-ray powder diffraction patterns," *Journal of Applied Crystallography*, vol. 14, no. 2, pp. 149–151, 1981.

[60] L. Wu, W. H. Lee, and J. Zhang, "First principles study on the electrochemical, thermal and mechanical properties of licoo2 for thin film rechargeable battery," *Materials Today: Proceedings*, vol. 1, no. 1, pp. 82–93, 2014.

[61] A. Saha, *Synthesis and characterization of grafted vanadium and co-graftedvanadium/zirconium mixed oxides on γ-alumina surface.* The University of Iowa, 2008.

[62] H. M. Sandvik, "Catalysis for control of methane slip in marine machinery-using a palladium based catalyst," Master's thesis, NTNU, 2016.

[63] W. Kohn and L. J. Sham, "Self-consistent equations including exchange and correlation effects," *Physical review*, vol. 140, no. 4A, p. A1133, 1965.

[64] O. Madelung, U. Rössler, M. Schulz *et al.*, "Ii-vi and i-vii compounds; semimagnetic compounds," *Berlin Heidelberg: Springer-Verlag*, vol. 41, pp. 1–5, 1999.

[65] B. Mamedov, E. Eser, H. Koç, and I. Askerov, "Accurate evaluation of the specific heat capacity of solids and its application to mgo and zno crystals," *International Journal of Thermophysics*, vol. 30, no. 3, pp. 1048–1054, 2009.

[66] W. Kohn and L. J. Sham, "Self-consistent equations including exchange and correlation effects," *Physical review*, vol. 140, no. 4A, p. A1133, 1965.

[67] J. P. Perdew, K. Burke, and M. Ernzerhof, "Generalized gradient approximation made simple," *Physical review letters*, vol. 77, no. 18, p. 3865, 1996.

[68] D. Vanderbilt, "Soft self-consistent pseudopotentials in a generalized eigenvalue formalism," *Physical review B*, vol. 41, no. 11, p. 7892, 1990.

[69] M. Barsoum and M. Barsoum, *Fundamentals of ceramics.* CRC press, 2002.

[70] D. Vanderbilt, "Soft self-consistent pseudopotentials in a generalized eigenvalue formalism," *Physical review B*, vol. 41, no. 11, p. 7892, 1990.

[71] A. Rao and K. Narender, "Studies on thermophysical properties of cao and mgo by-ray attenuation," *Journal of Thermodynamics*, vol. 2014, 2014.

[72] X. Tang and J. Dong, "Lattice thermal conductivity of mgo at conditions of earths interior," *Proceedings of the National Academy of Sciences*, vol. 107, no. 10, pp. 4539–4543, 2010.

[73] L. Wang, B. Hu, B. Li *et al.*, "Validity of fourier's law in one-dimensional momentum-conserving lattices with asymmetric interparticle interactions," *Physical Review E*, vol. 88, no. 5, p. 052112, 2013.

[74] P. Jund and R. Jullien, "Molecular-dynamics calculation of the thermal conductivity of vitreous silica," *Physical review B*, vol. 59, no. 21, p. 13707, 1999.

[75] A. J. Slifka, B. J. Filla, and J. Phelps, "Thermal conductivity of magnesium oxide from absolute, steady-state measurements," *Journal of research of the National Institute of Standards and Technology*, vol. 103, no. 4, p. 357, 1998.